



This is a repository copy of *Revisiting the transit timing and atmosphere characterization of the Neptune-mass planet HAT-P-26 b*.

White Rose Research Online URL for this paper:

<https://eprints.whiterose.ac.uk/204960/>

Version: Published Version

Article:

A-thano, N. orcid.org/0000-0001-7234-7167, Awiphan, S. orcid.org/0000-0003-3251-3583, Jiang, I.-G. orcid.org/0000-0001-7359-3300 et al. (11 more authors) (2023) Revisiting the transit timing and atmosphere characterization of the Neptune-mass planet HAT-P-26 b. *The Astronomical Journal*, 166 (6). 223. ISSN 0004-6256

<https://doi.org/10.3847/1538-3881/acfeeaa>

Reuse

This article is distributed under the terms of the Creative Commons Attribution (CC BY) licence. This licence allows you to distribute, remix, tweak, and build upon the work, even commercially, as long as you credit the authors for the original work. More information and the full terms of the licence here:

<https://creativecommons.org/licenses/>

Takedown

If you consider content in White Rose Research Online to be in breach of UK law, please notify us by emailing eprints@whiterose.ac.uk including the URL of the record and the reason for the withdrawal request.



eprints@whiterose.ac.uk
<https://eprints.whiterose.ac.uk/>



Revisiting the Transit Timing and Atmosphere Characterization of the Neptune-mass Planet HAT-P-26 b

Napaporn A-thano¹ , Supachai Awiphan² , Ing-Guey Jiang¹ , Eamonn Kerins³ , Akshay Priyadarshi³ , Iain McDonald^{3,4} , Yogesh C. Joshi⁵ , Thansuda Chulikorn⁶, Joshua J. C. Hayes³, Stephen Charles³, Chung-Kai Huang⁷ , Ronnakrit Rattanamala^{8,9}, Li-Chin Yeh¹⁰ , and Vik S Dhillon^{11,12}

¹ Department of Physics and Institute of Astronomy, National Tsing-Hua University, Hsinchu 30013, Taiwan; napaporn@gapp.nthu.edu.tw, jiang@phys.nthu.edu.tw

² National Astronomical Research Institute of Thailand, 260 Moo 4, Donkaew, Mae Rim, Chiang Mai 50180, Thailand; supachai@narit.or.th

³ Jodrell Bank Centre for Astrophysics, University of Manchester, Oxford Road, Manchester M13 9PL, UK

⁴ Department of Physical Sciences, The Open University, Walton Hall, Milton Keynes MK7 6AA, UK

⁵ Aryabhata Research Institute of Observational Sciences (ARIES), Manora Peak, Nainital 263001, India

⁶ Department of Physics, Faculty of Science, Chulalongkorn University, 254 Phayathai Road, Pathumwan, Bangkok 10330, Thailand

⁷ Institute of Astronomy and Astrophysics, Academia Sinica, No.1, Sec. 4, Roosevelt Road, Taipei 10617, Taiwan

⁸ PhD Program in Astronomy, Department of Physics and Materials Science, Faculty of Science, Chiang Mai University, Chiang Mai 50200, Thailand

⁹ Department of Physics and General Science, Faculty of Science and Technology, Nakhon Ratchasima Rajabhat University, Nakhon Ratchasima 30000, Thailand

¹⁰ Institute of Computational and Modeling Science, National Tsing-Hua University, Hsinchu 30013, Taiwan

¹¹ Department of Physics and Astronomy, University of Sheffield, Sheffield S3 7RH, UK

¹² Instituto de Astrofísica de Canarias, E-38205 La Laguna, Tenerife, Spain

Received 2023 March 2; revised 2023 September 18; accepted 2023 September 26; published 2023 November 3

Abstract

We present a transit-timing variation (TTV) and planetary atmosphere analysis of the Neptune-mass planet HAT-P-26 b. We present a new set of 13 transit light curves from optical ground-based observations and combine them with light curves from the Wide Field Camera 3 on the Hubble Space Telescope, the Transiting Exoplanet Survey Satellite, and previously published ground-based data. We refine the planetary parameters of HAT-P-26 b and undertake a TTV analysis using 33 transits obtained over seven years. The TTV analysis shows an amplitude signal of 1.98 ± 0.05 minutes, which could result from the presence of an additional $\sim 0.02 M_{\text{Jup}}$ planet at a 1:2 mean-motion resonance orbit. Using a combination of transit depths spanning optical to near-infrared wavelengths, we find that the atmosphere of HAT-P-26 b contains $2.4_{-1.6}^{+2.9}\%$ H_2O with a derived temperature of 590_{-50}^{+60} K.

Unified Astronomy Thesaurus concepts: [Exoplanet astronomy \(486\)](#); [Exoplanet atmospheres \(487\)](#); [Timing variation methods \(1703\)](#)

Supporting material: machine-readable table

1. Introduction

Over the last few decades, the study of exoplanetary systems has grown rapidly, as seen from the number of discovered planets and dedicated surveys. Of the more than 5000 discovered exoplanets so far, about 3000 transiting planets have been discovered¹³ by several different surveys, such as Kepler (Borucki et al. 2005), the Transiting Exoplanet Survey Satellite (TESS; Ricker et al. 2014), The Wide-Angle Search for Planets (WASP; Pollacco et al. 2006; Smith 2014), the Hungarian-made Automated Telescope Network (HATNet; Bakos et al. 2004, 2009), the Kilodegree Extremely Little Telescope (KELT; Pepper et al. 2007) survey, and the Next Generation Transit Survey (NGTS; Wheatley et al. 2018). In addition to the discovery of thousands of exoplanets, the transit technique can also be used to search for additional planets in the system via transit-timing variations (TTVs; Agol et al. 2005; Agol & Fabrycky 2018), and to characterize the compositions of planetary atmospheres via transmission spectroscopy (Seager & Sasselov 2000; Seager & Deming 2010).

Current and future detection and atmospheric characterization missions, including TESS, JWST (Pontoppidan et al. 2022), the PLANetary Transits and Oscillations (PLATO) survey (Rauer et al. 2014), and Atmospheric Remote-sensing Infrared Exoplanet Large-survey (ARIEL; Tinetti et al. 2018) herald a new era for exoplanetary research. TESS provides continuous, multi-epoch, high-precision light curves, which alone can be used to search for short-term TTVs (<5 yr). Since 2018, TESS has detected the TTV signals of a number of planets, including two new detections: AU Mic c (Wittrock et al. 2022) and TOI-2202 c (Trifonov et al. 2021).

For exoplanetary atmospheres, the Wide Field Camera 3 (WFC3) on the Hubble Space Telescope (HST) has been used for the detailed study of a number of exoplanets ranging from hot Jupiters to Neptune-sized planets and super-Earths (Kreidberg et al. 2014; Tsiaras et al. 2016a; Burt et al. 2021; Edwards et al. 2021; Brande et al. 2022; Glidic et al. 2022). Since the commencement of science operation in mid-2022, JWST has been used to study the chemical composition of exoplanetary atmospheres in the near-infrared. From the JWST Early Release Observations (ERO) program (Pontoppidan et al. 2022), observations from several JWST instruments have revealed the atmospheric compositions of several exoplanets (e.g., WASP-39 b; Rustamkulov et al. 2023).

While HST, Kepler, TESS, JWST, PLATO, and ARIEL are all designed to deliver high-quality data from space of exoplanets' physical and chemical properties, ground-based

¹³ From NASA exoplanet archive: <https://exoplanetarchive.ipac.caltech.edu/>.



Table 1
Summary of HAT-P-26 System’s Properties from Hartman et al. (2011)

Parameter	Value
Stellar Parameters	
M_*	$0.82 \pm 0.03 M_\odot$
R_*	$0.79 \pm 0.01 R_\odot$
T_*	5079 ± 88 K
$\log g_*$	4.56 ± 0.06 cgs
Metallicity [Z_*]	-0.04 ± 0.08
Planetary Parameters	
M_p	$0.059 \pm 0.007 M_{\text{Jup}}$
R_p	$0.565^{+0.072}_{-0.032} R_{\text{Jup}}$
T_{eq}	1001^{+66}_{-37} K
ρ_p	0.40 ± 0.10 g cm $^{-3}$
P (days)	$4.234516 \pm 2 \times 10^{-5}$
i (deg)	$88.6^{+0.5}_{-0.9}$
a/R_*	13.06 ± 0.83

observations remain critical for long-term monitoring of light-curve behavior. The Spectroscopy and Photometry of Exoplanet Atmospheres Research Network (SPEARNET) is a long-term statistical study of the atmospheres of hot transiting exoplanets using transmission spectroscopy. Its observations are supported by a globally distributed heterogeneous network of optical and infrared telescopes with apertures from 0.5 to 3.6 m, which can be combined with archival data from both ground- and space-based surveys. Our new transit-fitting code, *TransitFit* (Hayes et al. 2021), is designed for use with heterogeneous, multiwavelength, multiepoch, and multitelescope observations of exoplanet hosts and can fit global parametric models to entire data sets.

Since 2015, SPEARNET has monitored transits of HAT-P-26 b, which is a Neptune-mass planet orbiting its host, K1 dwarf HAT-P-26 ($V=11.74$), with a period of 4.234 days (Hartman et al. 2011). The stellar and planetary parameters of the HAT-P-26 system are given in Table 1. Transmission spectra of HAT-P-26 b were first studied by Stevenson et al. (2016). Using observations from Magellan and Spitzer, they reported that HAT-P-26 b is likely to have high metallicity, with a cloud-free upper atmosphere containing water and a 1000 Pa cloud deck. Wakeford et al. (2017) obtained observations with HST and the Spitzer Space Telescope, which showed a high-significance detection of H₂O and a metallicity approximately 4.8 times solar abundance.

MacDonald & Madhusudhan (2019) combined previous HST and Spitzer data of HAT-P-26 b with ground-based spectroscopic observations from the Magellan Low Dispersion Survey Spectrograph 3 (LDSS-3C; Stevenson et al. 2016). In the study, H₂O was detected with an abundance of 1.5% and O/H with an abundance 18.1 times solar. They also reported evidence for metal hydrides in the spectra with $>4\sigma$ confidence, with potential candidates identified as TiH, CrH, and ScH. The presence of metal hydrides in the atmosphere requires extreme conditions, such as the vertical transportation of material from the deep atmosphere or solid planetesimals containing heavy elements impacting the planet, which dissolve the elements into the He/H₂ envelope through shocks and fireballs.

Besides the study of transmission spectroscopy, HAT-P-26 b was examined for TTVs by von Essen et al. (2019). They performed follow-up photometric observation with the 2.15 m

Jorge Sahade Telescope, Argentina, as well as a 1.2 m robotic telescope (STELLA) and the 2.5 m Nordic Optical Telescope (NOT), both located on the Canary Islands. The observed transits showed a ~ 270 epoch periodic timing variation with an amplitude of ~ 4 minutes, which might be caused by a third body in the system.

In this work, we present new ground-based SPEARNET multiband photometric follow-up observations of 13 transits of HAT-P-26 b. These data are combined with TESS, HST, and available published photometric data to constrain the planetary physical parameters, investigate the planetary TTV signal, and constrain the atmospheric model. Our observational data are presented in Section 2. The light-curve analysis is described in Section 3. A new linear ephemeris and a frequency study of TTVs are presented in Section 4. In Section 5, the atmospheric composition of HAT-P-26 b is analyzed. Finally, the discussion and conclusions are in Section 6.

2. Observational Data

Since the discovery of HAT-P-26 b in 2011, the planetary system has been monitored by a number of campaigns, as discussed in Section 1. In this work, we present the data from our observations (13 transit light curves) and previously published data (69 transit light curves). The details of each observational data set are described below.

2.1. SPEARNET Observations and Data Reduction

Between 2015 March and 2022 May, photometric follow-up observations of HAT-P-26 b were obtained using the SPEARNET telescopes network (Figure 1). Time-series photometry of thirteen transits, including eight full and five partial transits, were obtained. The observation log is given in Table 2. The facilities used to obtain our data were as follows:

1. 2.4 m Thai National Telescope (TNT) located at the Thai National Observatory (TNO), Thailand. During 2015–2019, five full transits and two partial transits of HAT-P-26 b were obtained by the TNT. The observations were conducted using ULTRASPEC (Dhillon et al. 2014), a high-speed frame-transfer EMCCD 1024×1024 pixel camera, with a field of view of 7.68×7.68 arcmin².
2. 0.5 m Thai Robotic Telescope located at TNO (TRT-TNO), Thailand. We observed one full transit and one partial transit of HAT-P-26 b between 2017 and 2018 with the Schmidt–Cassegrain TRT-TNO. (Currently, the facility is upgraded to a 1 m telescope.) The observations were performed using an Apogee Altra U9000 3056×3056 pixel CCD camera. The field of view is about 58×58 arcmin².
3. 0.7 m Thai Robotic Telescope at the Gao Mei Gu Observatory (TRT-GAO), China. One partial transit of HAT-P-26 b was obtained by TRT-GAO in 2017. TRT-GAO is equipped with an Andor iLon-L 936, with a 2048×2048 pixel CCD camera. The field of view is 20.9×20.9 arcmin².
4. 0.7 m Thai Robotic Telescope at the Sierra Remote Observatories (TRT-SRO), USA. In 2022, TRT-SRO obtained two full and one partial transit. We observed HAT-P-26 b with the Andor iKon-M 934 1024×1024 pixel CCD camera. The field of view is 10×10 arcmin².



Figure 1. The locations and sizes of the telescopes in SPEARNET.

Table 2
Observation Details of HAT-P-26 b's Transits Using the Telescopes within SPEARNET

Observation Date	Epoch	Telescope	Filter	Exposure Time (s)	Number of Images	Total Duration of Observation (hr)	PNR (%)	Transit Coverage
2015 Mar 05	421	2.4 m TNT	i'	1.90	3892	2.49	0.09	Egress only
2015 Mar 22	425	2.4 m TNT	i'	2.47	6683	4.92	0.12	Full
2016 Feb 11	502	2.4 m TNT	g'	9.23	1574	4.19	0.07	Full
2017 Mar 15	596	0.7 m	R	40	235	3.65	0.19	Ingress only
2017 Mar 15	596	TRT-GAO						
		0.5 m	I	30	270	3.13	0.17	Ingress only
2018 Mar 27	685	TRT-TNO						
		2.4 m TNT	g'	4.53	4465	5.77	0.35	Full
2018 Mar 27	685	0.5 m	R	40	216	2.93	0.21	Full
2018 Apr 13	689	TRT-TNO						
		2.4 m TNT	z'	2.68	4590	4.51	0.17	Full
2019 Mar 05	766	2.4 m TNT	r'	2.98	5493	4.71	0.10	Full
2019 Apr 25	778	2.4 m TNT	z'	4.86	2481	4.12	0.14	Egress only
2022 Mar 23	1029	0.7 m TRT-SRO	R	30	353	4.01	0.24	Full
2022 May 13	1041	0.7 m TRT-SRO	I	30	273	3.32	0.40	Full
2022 May 30	1045	0.7 m TRT-SRO	R	30	226	2.10	0.25	Egress only

Note. Epoch = 0 is the transit on 2010 April 18. PNR is the photometric noise rate (Fulton et al. 2011).

All the science images of HAT-P-26 b were preprocessed using standard tasks from IRAF¹⁴ (Tody 1986, 1993). Astrometric calibrations were performed using *Astrometry.net* (Lang et al. 2010), and aperture photometry was performed by Source Extractor (Bertin & Arnouts 1996). We use *mag_auto*, which is Kron-like automated scaled aperture magnitude, with a Kron factor of 2.5 and a minimum radius of 3.5. Reference stars were selected from nearby stars that were within ± 3 mag of HAT-P-26 and that did not exhibit strong brightness variation. The sigma clipping algorithm, with a 5σ threshold, was employed to remove the outlier points in the light curves. To produce the light curves, the flux of HAT-P-26 was divided by the sum of the flux from the selected reference stars. Image time stamps were converted to Barycentric Julian Date in Barycentric Dynamical Time (BJD_{TDB}) using

barycorrpy (Kanodia & Wright 2018). The normalized light curves are available in a machine-readable form in Table 4.

2.2. Existing Ground-based Data

We used 16 additional light curves from two previous ground-based studies. First, five i' -band transits of HAT-P-26 b were obtained using KeplerCam on the FLWO 1.2 m telescope obtained by Hartman et al. (2011).¹⁵ Second, we used 11 Cousins- R transits obtained by von Essen et al. (2019) who used the 2.15 m Jorge Sahade Telescope at the Complejo Astronómico El Leoncito (CASLEO), the 2.5 m NOT at La Palma, Spain, and the 1.2 m STELLA at Tenerife, Spain.¹⁶ These are summarized in Table 3. Combining these data with our observations of 13 transits, we use ground-based

¹⁴ IRAF is distributed by the National Optical Astronomy Observatories, which are operated by the Association of Universities for Research in Astronomy, Inc., under a cooperative agreement with the National Science Foundation. For more details, <http://iraf.noao.edu/>.

¹⁵ Downloaded from the CDS: <https://cdsarc.cds.unistra.fr/viz-bin/cat/J/ApJ/728/138>

¹⁶ Downloaded from the CDS: <https://cdsarc.cds.unistra.fr/viz-bin/cat/J/A+A/628/A116>

Table 3

Summary of HAT-P-26 b's Transits Light Curves Taken from Ground-based Archive Data

Observation Date	Telescope	Filter
Hartman et al. (2011)		
2010 Jan 05 [*]	KeplerCam/FLWO 1.2 m	<i>i'</i>
2010 Mar 31 [*]	KeplerCam/FLWO 1.2 m	<i>i'</i>
2010 Apr 04	KeplerCam/FLWO 1.2 m	<i>i'</i>
2010 May 08	KeplerCam/FLWO 1.2 m	<i>i'</i>
2010 May 25	KeplerCam/FLWO 1.2 m	<i>i'</i>
von Essen et al. (2019)		
2015 Mar 30	2.15 m CASLEO	<i>R</i>
2015 Apr 12	2.5 m NOT	<i>R</i>
2015 Apr 16	2.15 m CASLEO	<i>R</i>
2015 May 20 [*]	2.5 m NOT	<i>R</i>
2015 Jun 06	2.5 m NOT	<i>R</i>
2015 Jun 23	2.5 m NOT	<i>R</i>
2016 May 14 [*]	2.15 m CASLEO	<i>R</i>
2017 May 13 [*]	2.15 m CASLEO	<i>R</i>
2017 May 30	2.15 m CASLEO	<i>R</i>
2017 Jun 16 [*]	2.15 m CASLEO	<i>R</i>
2018 Jul 01 [*]	1.2 m STELLA	<i>R</i>

Note. * Only part of the transit was observed.

photometry from 29 transits obtained over a span of 20 yr within six broad photometric bands.

2.3. HST WFC3 Grism Data

In addition to ground-based observations, HST observed three transits of HAT-P-26 b using WFC3 (Wakeford et al. 2017). Two transits were observed using the G141 grism (1.1–1.7 μm) on 2016 March 12 and 2016 May 02. Another transit was observed using the G102 grism (0.8–1.1 μm) on 2016 October 16.

The raw spectra were reduced using the *Iraclis* package, a Python package for the WFC3 spectroscopic reduction pipeline (Tsiaras et al. 2016b, 2016a).¹⁷ The HST data from the G141 grism spectra were binned into 18 wavelength bins, while the G102 grism spectra were binned into 14 wavelength bins. In total, 50 light curves were obtained from HST/WFC3. We discarded the data from the first orbit of each visit and the first exposure of each orbit as the data exhibit a stronger wavelength-dependent ramp during these epochs.

2.4. TESS Data

TESS observed three transit light curves of HAT-P-26 b in Sector 50 (2022 March–April). We used the Pre-Search Data Conditioning (PDC) light curves (Smith et al. 2017a, 2017b), which were the calibrated light curves from the Science Processing Operation Center (SPOC) pipeline (Jenkins et al. 2016).¹⁸ The dilution and background-corrected PDCSAP light curves from the SPOC pipeline are used in this work.

Table 4

A Sample of the Detrended and Normalized Photometry for HAT-P-26 b Using the Telescopes within SPEARNET

Epoch	BJD	Normalized Flux	Normalized Flux Uncertainty
421	2,457,087.35923	0.995	0.004
	2,457,087.35925	0.996	0.005
	2,457,087.35927	0.998	0.005
	2,457,087.35934	1.000	0.004
	2,457,087.35936	0.996	0.004
...
425	2,457,104.23686	0.990	0.004
	2,457,104.23689	1.002	0.004
	2,457,104.23694	0.990	0.004
	2,457,104.23700	1.011	0.004
	2,457,104.23703	1.002	0.004
...
502	2,457,430.29378	1.002	0.002
	2,457,430.29388	1.002	0.002
	2,457,430.29420	0.998	0.002
	2,457,430.29431	1.002	0.002
	2,457,430.29452	0.999	0.002
...
...

Note. The transits were all detrended with a second-order polynomial function in *TransitFit*. Epoch = 0 is the transit on 2010 April 18.

(This table is available in its entirety in machine-readable form.)

3. Light-curve Modeling

HAT-P-26 b has been observed by several observing campaigns, which report subtly different planetary physical parameters. The differences can arise from different modeling assumptions, such as the treatment of limb darkening. In this present study, the physical parameters of HAT-P-26 b are reanalyzed using the *TransitFit* (Version 3.0.9), a Python package that can simultaneously fit multifilter, multiepoch exoplanet transit observations (Hayes et al. 2021). *TransitFit* models transits using *batman* (Kreidberg 2015) and performs fitting using the dynamic nested-sampling routine from *dynesty* (Speagle 2020).

The combined ground and space data sets comprise 85 separate light curves spanning a range of epochs and wavelengths. We fit and detrend all of them simultaneously using *TransitFit*. *TransitFit* performed nested-sampling retrieval with 1000 live points and a slice sampling of 10. During the retrieval, each transit light curve was individually detrended using different detrending functions: for each ground-based and TESS observations, we used individual second-order polynomial detrending functions. For the HST/WFC3 data sets, the data were detrended using a model similar to Kreidberg et al. (2018b), specifically

$$F_{\text{sys}} = (S + v_1 t_{\text{visit}} + v_2 t_{\text{visit}}^2)(1 - e^{-a t_{\text{orb}} - b}), \quad (1)$$

where F_{sys} is the signal from the systematics, while $S = 1$ and s for forward and reverse scans, respectively. The parameters s , v_1 , v_2 , a , and b are all detrending coefficients, where s , a , and b account for the ramp-up systematic across all the light curves, while v_1 and v_2 are second-order polynomial detrending functions used to model the visit-long trends. The astrophysical

¹⁷ Downloaded from Exo.MAST: <https://exo.mast.stsci.edu/>.

¹⁸ Downloaded from the Mikulski Archive for Space Telescopes: <https://archive.stsci.edu/>.

Table 5The Initial Parameters and Priors Used to Model the Planetary Parameters Modeling with `TransitFit`

Parameter	Priors	Prior Distribution
P (days)	4.234516	Fixed
T_0 (BJD)	2455304.65122 ± 0.01	Gaussian
i (deg)	88.0 ± 0.5	Gaussian
a/R_*	13 ± 1	Gaussian
R_p/R_*	(0.06, 0.08)	Uniform
e	0	Fixed
T_* (K)	4700	Fixed
Z_*	-0.06	Fixed
$\log(g_*)$	4.5	Fixed

Note. The priors of P , T_0 , i , and a/R_* are set to the values in Hartman et al. (2011).

signal (F_{sig}) can be obtained by the division of the observed flux (F_{obs}) and the systematic signal (F_{sys}). The HST detrending function was defined as a custom detrending function in `TransitFit`. The normalized light curves with their observational uncertainties are available in a machine-readable form in Table 4.

HAT-P-26 b is assumed to be in a circular orbit. We find a stellar effective temperature for HAT-P-26 of $T_* = 4700 \pm 100$, determined from the Python Stellar Spectral Energy Distribution package,¹⁹ a tool set designed to allow the user to create, manipulate, and fit the spectral energy distributions of stars based on publicly available data (McDonald et al. 2009, 2012, 2017). To create the stellar SED, we obtained the available photometry, which consists of G , G_{BP} , and G_{RP} magnitudes from Gaia, g' , r' , i' , z' , y' magnitudes from the Panoramic Survey Telescope and Rapid Response System (Pan-STARRS), near-ultraviolet (NUV) magnitudes from the Galaxy Evolution Explorer (GALEX), B , V , g' , r' , i' from the AAVSO Photometric All-Sky Survey (APASS), JHK magnitudes from the Two Micron All Sky Survey (2MASS), and W1–W3 magnitudes from the Wide-field Infrared Survey Explorer (WISE). BT-Settl model atmospheres (Allard et al. 2011; Allard 2014) were used.

The host metallicity, $Z_* = -0.06 \pm 0.10$, and surface gravity, $\log(g_*) = 4.5 \pm 0.1$, are obtained from the Gaia EDR3 catalog.²⁰ To fit ground-based, TESS, and HST light curves, we fixed the orbital period (P) to 4.234516 days, which was adopted from Hartman et al. (2011), and used the ability of `TransitFit` to account for TTVs by using the `allow_TTV` function, in order to find the midtransit time, T_m , for each epoch. The parameters of inclination, i , semimajor axis a , and planet-to-host radius ratio, R_p/R_* were allowed to vary freely. The priors of each fitting parameter, the epoch of midtransit, T_0 , together with i , a , and R_p for each wave band, are given in Table 5.

The light curves of HAT-P-26 b were phase folded to center T_0 at a phase of 0.5, and the best-fit models and residuals are shown in Figures 2, 3, and 4. The derived planetary parameters for HAT-P-26 b from `TransitFit` are compared with the results from previous studies in Table 6. HAT-P-26 b has $i = 87.82^\circ \pm 0.05^\circ$ with a host separation of $12.51 \pm 0.07 R_*$ as shown in Table 6. These values exhibit a difference of $\sim 1\sigma$

compared to the previous published measurements. Individual SPEARNET light curves of HAT-P-26 b are shown in Figures A1 and A2 (see Appendix A).

The discrepancies between our fitting results and previous measurements of the inclination and host separation might be caused by missing ingresses or egresses of transits or interruptions during a transit due to weather in our ground-based light curves. Therefore, we perform another fitting analysis using the ground-based light curves, which have data during both ingress and egress plus at least 20 minutes of an out-of-transit baseline. We defined these light curves as “full light curves.” The fitting shows that the full light curves provide the same planetary parameters within 2σ of all light curves fitting (Table 6). This test ensures that the fitting results are not biased by the inclusion of partial transit light curves. Since there are no significant differences observed between the fitting results obtained from the analysis of all light curves and just the full light curves, we focus on the results derived from the fitting with all light curves in this study.

Furthermore, an exploration into the observed noise within the light curves was undertaken by examining the normalized rms behavior when the light curve is binned in time, following the methodology outlined in Kreidberg et al. (2018a). The hypothetical white noise curve should decrease by a factor of \sqrt{N} , where N represents the number of points per bin. The normalized rms values were calculated for both the ground-based and HST light curves, and the results are shown in Figures 5 and 6. The overall trend observed in the 2.4 m TNT data indicates the presence of white noise. Nevertheless, as the bin size increases, there is evidence of red noise, particularly within the i' filter. For the TRT data, most of the light curves exhibit characteristics of white noise, except for the I -filter data from TRT-TNO, which display an increasing degree of red noise with larger bin sizes. Regarding the HST/WFC3 data collected from the G102 and G141 grisms, the analysis reveals a prevalence of white noise throughout the data set. However, in the G102 data, some instances of red noise become apparent in the large bin size of the light curves when binned within the initial wavelength range (0.8–0.9 μm). Additionally, the publicly available light curves in the R band also show the existence of time-correlated noise. This presence of red noise within these specific data and wavelength bands might potentially be attributed to the quality of the data obtained during those observations.

Midtransit times (T_m) for each transit and the corresponding epoch number, E , are given in Table 7 and discussed in Section 4. The values of R_p/R_* are shown in Table 8. We can now compare the R_p/R_* values obtained from `TransitFit` with those from previous studies. The transit depths obtained from `TransitFit` exhibit variations at the $\sim 5\sigma$ level, which can be explained by wavelength-dependent variations of the atmospheric transmission spectrum. For instance, in the i' filter, our observation of $R_p/R_* = 0.0716 \pm 0.0001$ is consistent within the 2σ range of the value reported by Hartman et al. (2011; 0.0737 ± 0.0012). However, in the R filter, we found a shallower transit depth ($R_p/R_* = 0.0698 \pm 0.0002$) compared to the measurement provided by von Essen et al. (2019; 0.07010 ± 0.00016). For the HST filters, the R_p/R_* values from `TransitFit` are consistent with the values provided by Wakeford et al. (2017). In the case of TESS, the fitted value for R_p/R_* is calculated to be 0.0711 ± 0.0007 , which

¹⁹ <https://explore-platform.eu/>

²⁰ Gaia archive: <https://archives.esac.esa.int/gaia>.

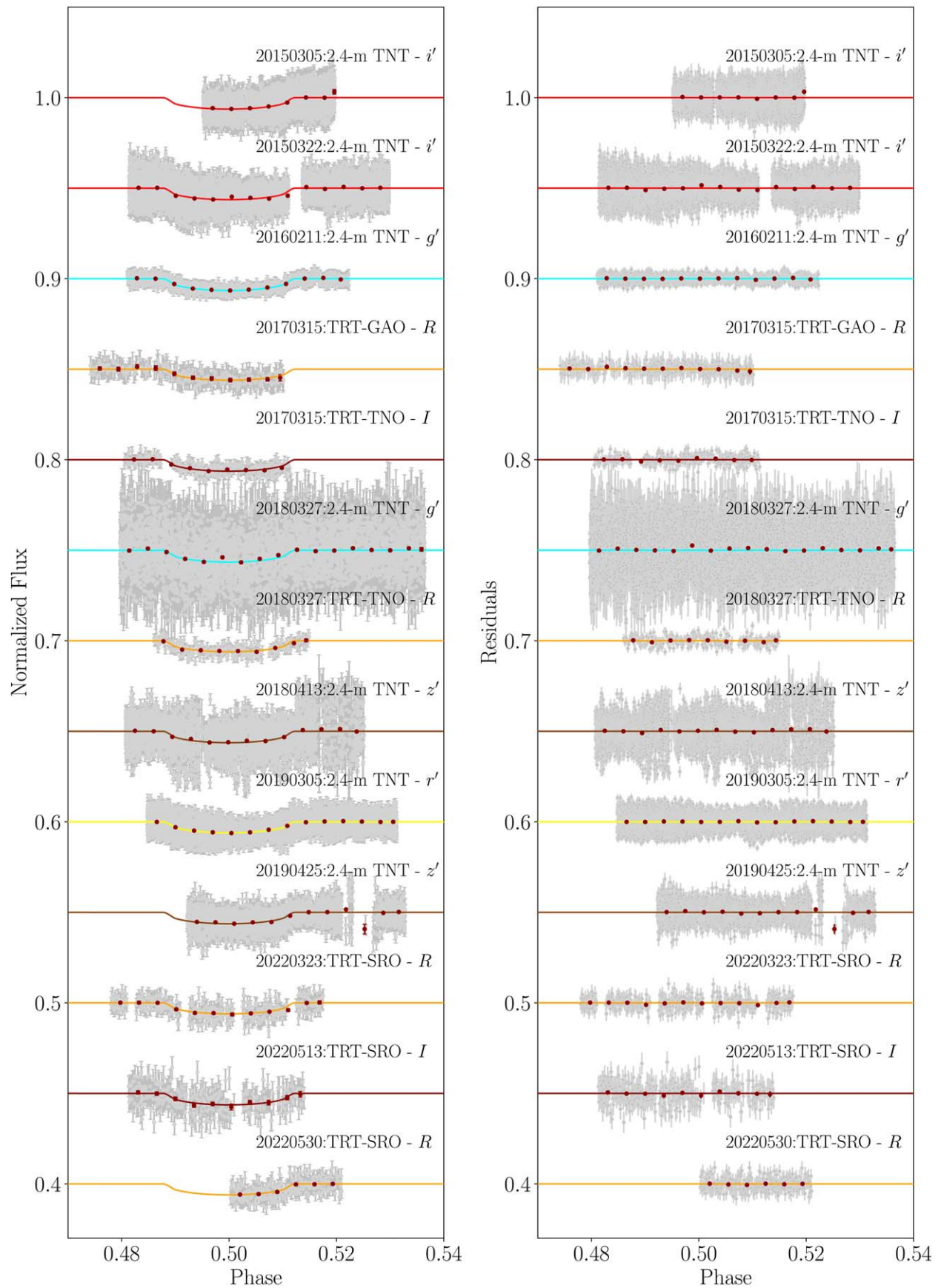


Figure 2. Left panels: normalized, phased-folded HAT-P-26 b transit light curves observed using the SPEARNET telescope network (gray dots) with the best-fitting model from *TransitFit* (solid lines). The red dots show the light curves binned into 5 minute intervals. Right panels: the corresponding residual light curves after the models are subtracted. Both the light curves and the residuals have arbitrary vertical offsets for clarity.

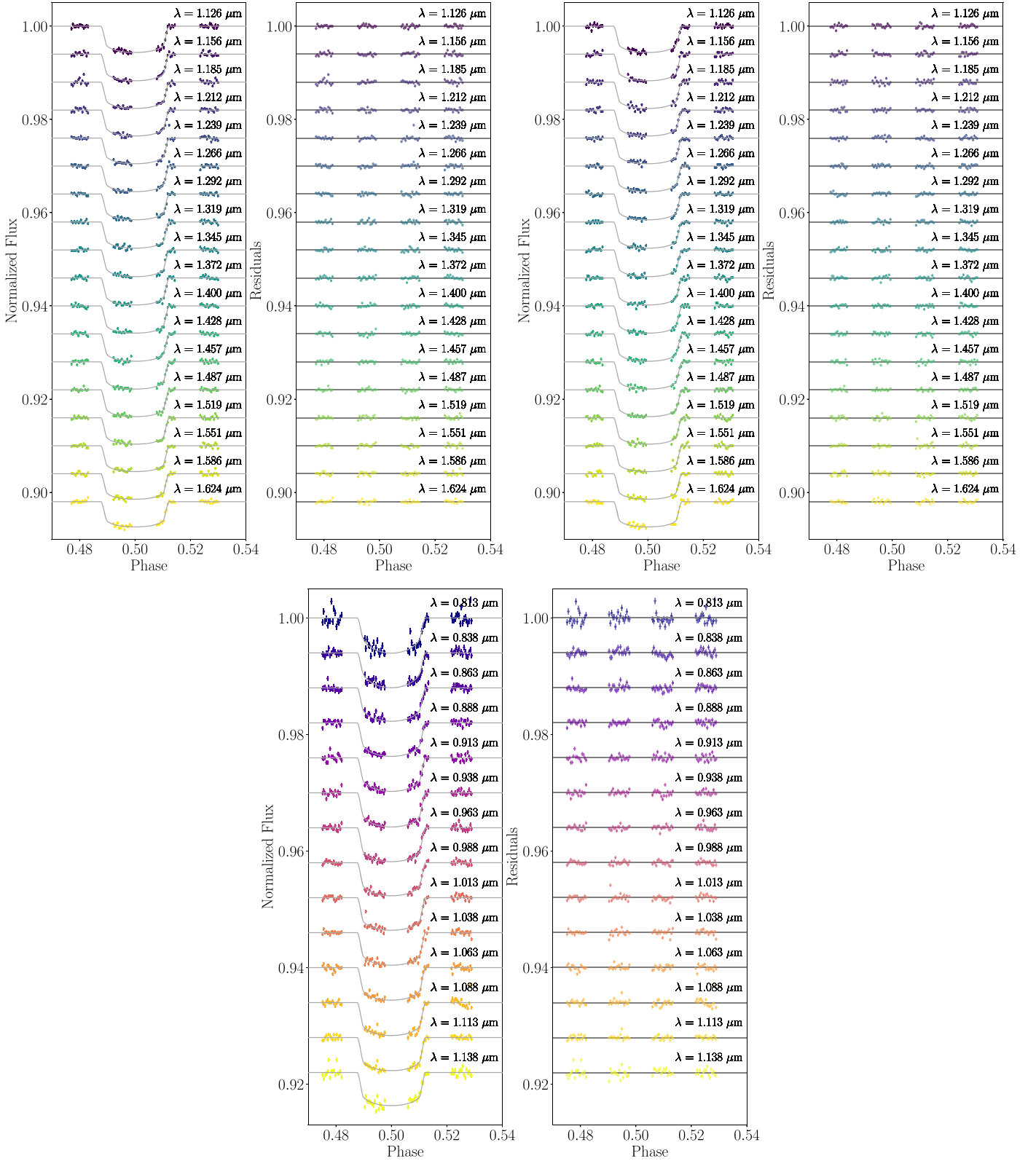


Figure 3. Normalized, phased-folded HAT-P-26 b transit light curves from HST/WFC3, reduced using the *traclis* package (dots). Three sets of observations are shown, with the light curves and *TransitFit* models in the left-hand panels, and the corresponding residual differences in the right-hand panels. The top-left, top-right, and bottom pairs of panels respectively show the G141 grism observations from 2016 March 12, the G141 grism observations from 2016 May 02, and the G102 grism observations from 2016 October 16. The light curves and the residuals have arbitrary offsets for clarity.

aligns with results obtained at the other wavelengths. These transit depths are used for the atmospheric modeling in Section 5.

For the limb-darkening coefficients (LDCs), the quadratic LDCs from Hartman et al. (2011) were $u_0 = 0.386$ and $u_1 = 0.258$, adopted from the tabulations by Claret (2004) for

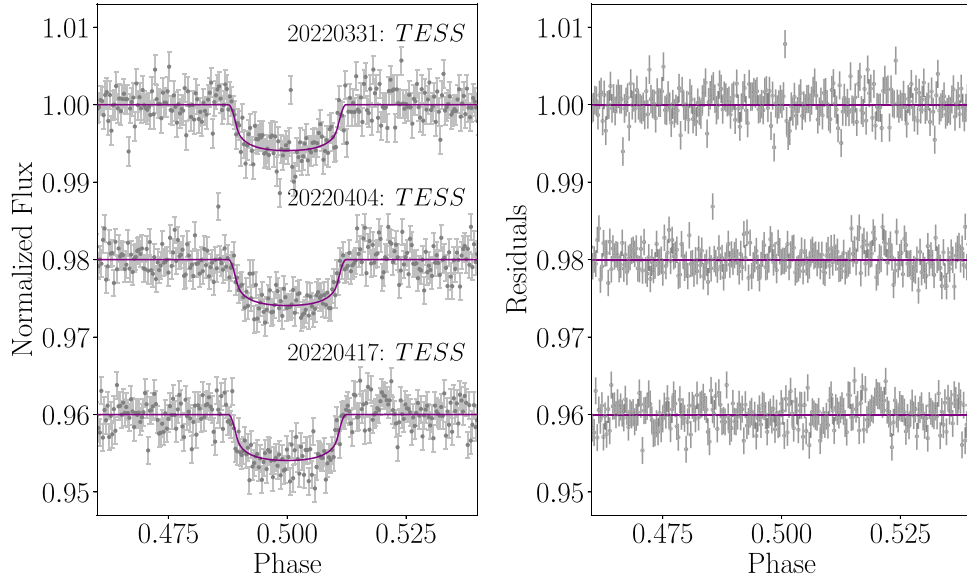


Figure 4. Normalized, phased-folded HAT-P-26 b transit light curves from TESS (gray dots, left panels) with the best-fitting model from `TransitFit` (solid lines). Their corresponding residuals are shown in the right panels. The light curves and the residuals have arbitrary offsets for clarity.

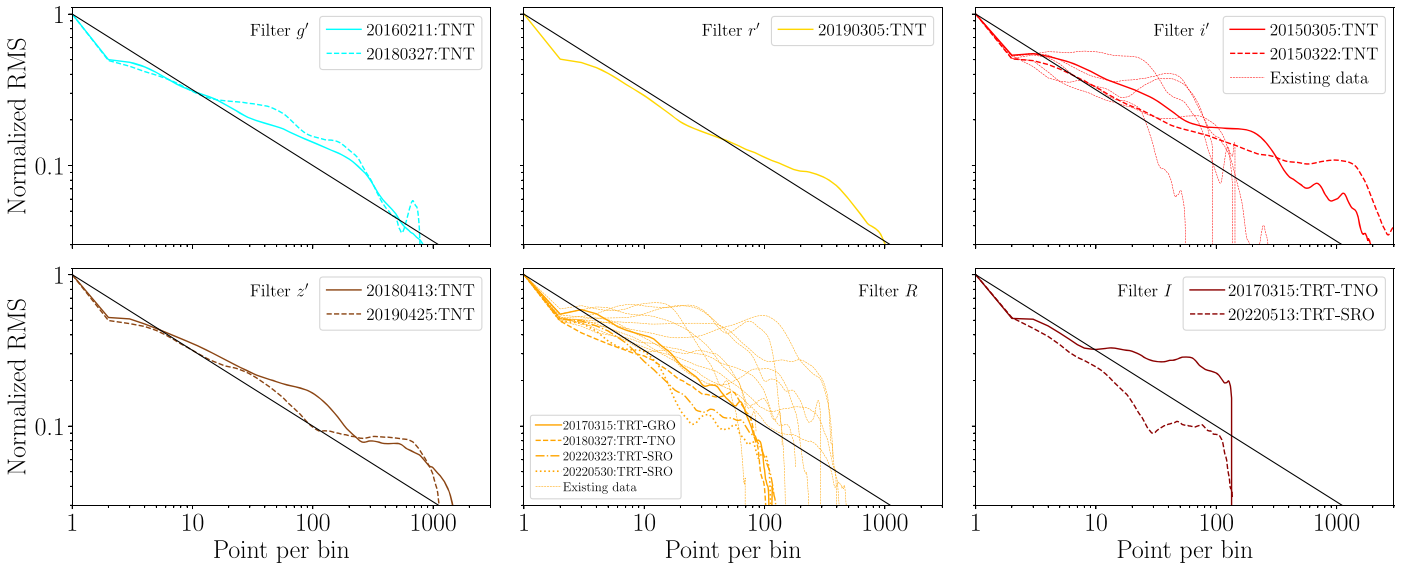


Figure 5. Normalized rms plots for all ground-based residual light curves from both our observations and existing data fit as a function of the number of points per bin. The observation data are shown in g' (blue), r' (yellow), R (orange), i' (red), I (dark red), and z' (brown).

Table 6
The Physical Parameters of HAT-P-26 b from the `TransitFit` Package and Values from the Literature

Parameter	Hartman et al. (2011)	Stevenson et al. (2016)	von Essen et al. (2019)	This work	
				All LCs	Full LCs
P (days)	$4.234516 \pm 2 \times 10^{-5}$	$4.2345023 \pm 7 \times 10^{-7}$	$4.23450236 \pm 3 \times 10^{-8}$	4.234516^*	
i (deg)	$88.6^{+0.5}_{-0.9}$	87.3 ± 0.4	87.31 ± 0.09	87.82 ± 0.05	87.72 ± 0.05
a/R_*	13.06 ± 0.83	11.8 ± 0.6	12.05 ± 0.13	12.51 ± 0.07	12.53 ± 0.05

Note. *Value used is adopted from Hartman et al. (2011). Light curves are abbreviated as LCs in the final two columns.

the i' filter, based on a stellar temperature of $T_* = 5079 \pm 88$ K and metallicity of $Z_* = -0.04 \pm 0.08$. Similar quadratic LDCs in von Essen et al. (2019) were taken from the R filter tabulated

values of Claret (2000) as $u_0 = 0.514$ and $u_1 = 0.218$, based on $T_* = 5000$ K and $Z_* = 0$. Due to the broad range of wave bands analyzed in this work, the coupled fitting mode in

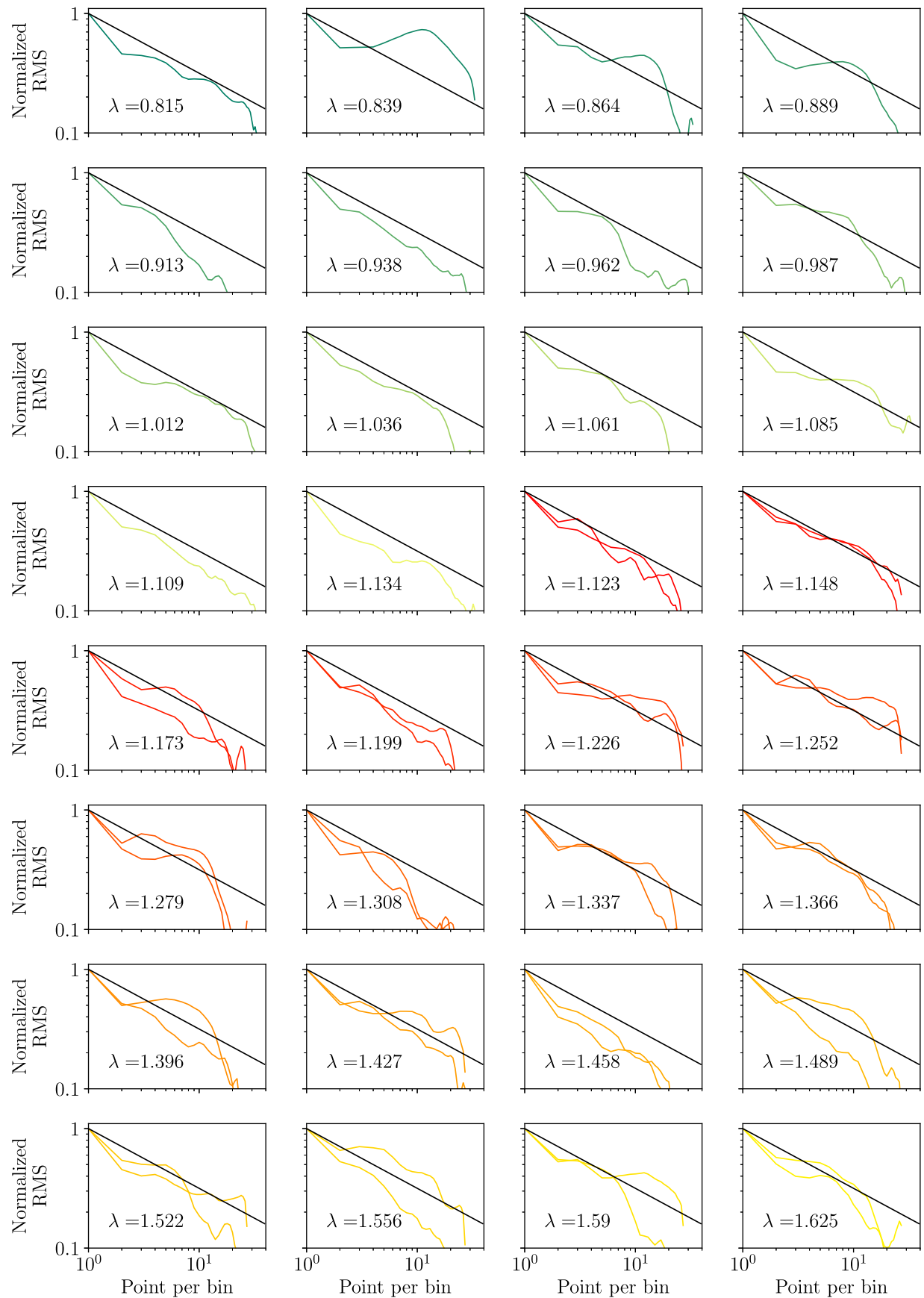


Figure 6. Normalized rms plots for the HST residual light curves fit as a function of the number of points per bin. The observations from HST/WFC3 G102 and HST/WFC3 G141 are shown in green and red, respectively.

Table 7
HAT-P-26 b's Midtransit Times (T_m) and Timing Residuals ($O - C$)

Epoch	$T_m + 2,450,000$ (BJD _{TDB})	$(O - C)_{33}$ (days)	$(O - C)_{39}$ (days)	Ref.
-105	4860.02786 ± 0.00147 ^a	...	-0.00146	(a)
-24	5203.02521 ± 0.00031	0.00116	0.00118	(a)
-4	5287.71490 ± 0.00050	0.00080	0.00082	(a)
-3	5291.94879 ± 0.00019	0.00019	0.00021	(a)
0	5304.65218 ± 0.00003 ^a	...	0.00009	(b)
5	5325.82444 ± 0.00015	-0.00019	-0.00016	(a)
9	5342.76192 ± 0.00025	-0.00072	-0.00070	(a)
260	6405.62370 ± 0.0009 ^a	...	0.00094	(b)
293	6545.36220 ± 0.0003 ^a	...	0.00085	(b)
421	7087.37845 ± 0.00032	0.00074	0.00077	(f)
425	7104.31554 ± 0.00023	-0.00018	-0.00014	(f)
427	7112.78490 ± 0.00057	0.00017	0.00021	(d)
430	7125.48903 ± 0.00071	0.00079	0.00083	(d)
431	7129.72198 ± 0.00090	-0.00076	-0.00073	(d)
431	7129.72248 ± 0.00017 ^a	...	-0.00022	(b)
439	7163.59815 ± 0.00054	-0.00061	-0.00057	(d)
443	7180.53670 ± 0.00041	-0.00007	-0.00004	(d)
447	7197.47394 ± 0.00024	-0.00084	-0.00081	(d)
498	7413.43284 ± 0.00017 ^a	...	-0.00154	(c)
502	7430.37175 ± 0.00025	-0.00068	-0.00064	(f)
509	7460.01268 ± 0.00005	-0.00126	-0.00122	(c)
521	7510.82651 ± 0.00005	-0.00146	-0.00143	(c)
524	7523.53019 ± 0.00099	-0.00129	-0.00125	(d)
546	7616.68959 ± 0.00007	-0.00095	-0.00091	(c)
596	7828.41858 ± 0.00093	0.00291	0.00295	(f)
610	7887.70232 ± 0.00420	0.00362	0.00366	(d)
614	7904.63921 ± 0.00079	0.00249	0.00253	(d)
618	7921.57729 ± 0.00045	0.00257	0.00260	(d)
685	8205.28614 ± 0.00047	-0.00026	-0.00022	(f)
689	8222.22421 ± 0.00022	-0.00020	-0.00016	(f)
690	8226.45946 ± 0.00065	0.00055	0.00059	(d)
766	8548.28051 ± 0.00017	-0.00060	-0.00056	(f)
778	8599.09456 ± 0.00038	-0.00058	-0.00054	(f)
1029	9661.95548 ± 0.00078	0.00018	0.00023	(f)
1031	9670.42414 ± 0.00076	-0.00016	-0.00011	(e)
1032	9674.65912 ± 0.00078	0.00032	0.00037	(e)
1035	9687.36206 ± 0.00075	-0.00026	-0.00020	(e)
1041	9712.77013 ± 0.00171	0.00080	0.00086	(f)
1045	9729.70826 ± 0.00091	0.00092	0.00097	(f)

Notes. $(O - C)_{33}$ are calculated from Equation (3), which considers the 33 midtransit times modeled with `TransitFit`. $(O - C)_{39}$ is calculated from Equation (4), which include six midtransit times from the literature but which do not have published raw light curves. Epoch = 0 is the transit on 2010 April 18. Data sources: (a) Hartman et al. (2011), (b) Stevenson et al. (2016), (c) Wakeford et al. (2017), (d) von Essen et al. (2019), (e) TESS, and (f) this study. ^a T_m adopted from the literature.

`TransitFit` was used to determine the LDCs for each filter. The LDC fitting is conditioned using priors generated by the Limb Darkening Toolkit (LDTk; Parviainen & Aigrain 2015) for each filter response, based on PHOENIX²¹ stellar atmosphere models (Husser et al. 2013). Our previously determined host star parameters, including T_* , $\log(g)$, and Z_* , are adopted for the LDC calculations. The LDCs for different filters from the coupled fitting mode are given in Table 8.

To validate our fitted LDC values, we compare them against those acquired through the Python-based LDTk (`PyLDTk`) and

the Exoplanet Characterization ToolKit (`ExoCTK`;²² Bourque et al. 2021). Our fitted LDC values, the `PyLDTk` and `ExoCTK` LDCs are plotted in Figure 7. Although there is no overlap between the limb-darkening values obtained from `TransitFit` and those from `PyLDTk` or `ExoCTK`, particularly within the broadband optical filters, consistent trends are still apparent across all sources. To demonstrate that the discrepancy in the LDCs does not significantly impact the determination of the planetary system parameters, especially the planetary radii, we conducted an analysis with the LDCs fixed at the `PyLDTk` values. This analysis provided values of $i = 87.92^\circ \pm 0.06^\circ$ and $a/R_* = 12.55 \pm 0.07$, which align with the results from the fitting of LDCs. The midtransit times fall within the 1σ range of the previous analysis. The planetary radii calculated with the fixed LDCs are presented in Table 8. These radii exhibit the same trend, with a slightly larger size that remains within the 1σ range of the analysis involving fitting LDCs, as shown in Figure 8. Therefore, we can confirm that these discrepancies do not effect the TTV and atmospheric analyses, which are based on the data obtained from the fitted LDCs in this work.

4. Transit-timing Analysis

4.1. A Refined Ephemeris

The midtransit times of the 33 epochs obtained from `TransitFit`, and listed in Table 7, are considered for our timing analysis. The midtransit times were fitted by a linear ephemeris model, using a constant period as

$$T_m^c(E) = T_{0,l} + P_l \times E, \quad (2)$$

where $T_{0,l}$ and P_l are the reference time and the orbital period of the linear ephemeris model, respectively, and E is the epoch number, where $E = 0$ represents the transit on 2010 April 18. $T_m^c(E)$ is the calculated midtransit time at a given epoch E .

To find the best-fit parameters from the model, we used `emcee` (Foreman-Mackey et al. 2013) to perform a Markov Chain Monte Carlo (MCMC) fit with 50 chains and 10^5 MCMC steps. The new linear ephemeris was defined as

$$T_m^c(E) = 2455304.65211_{-0.00035}^{+0.00036} + 4.234503_{-0.00001}^{+0.00001}E. \quad (3)$$

The reduced chi-square of the linear fit is $\chi_{\text{red}}^2 = 55$ with 31 degrees of freedom. The Bayesian information criterion, $BIC = \chi^2 + k \ln n = 1698$, where k is the number of free parameters and n is the number of data points. A corner plot indicating the MCMC posterior probability distribution of the parameters is shown in Figure (B1). The obtained period from $O - C$ is consistent with the periods provided by Stevenson et al. (2016) and von Essen et al. (2019). However, the value differs from our prior period in the `TransitFit`, which was adopt from Hartman et al. (2011), by ~ 1 s. The difference does not affect our fitted timing as we used the `allow_TTV` function in the `TransitFit`. For the fitted physical parameters, the effects of the different periods are small and negligible. Using the new ephemeris, we constructed an $O - C$ diagram (Figure 9(b)), which shows the residual differences between the timing data and Equation (3).

In addition to the midtransit times obtained from `TransitFit`, there are six transits whose light curves are not

²¹ PHOENIX: <http://phoenix.astro.physik.uni-goettingen.de/>.

²² `ExoCTK` limb-darkening calculator: <https://exoctk.stsci.edu/limb-darkening>.

Table 8

The Planet-to-star Radius Ratio (R_p/R_*) for Both Models with Fitted LDCs and Fixed LDCs, and the Quadratic LDCs of HAT-P-26 b in different Filters, as Obtained by `TransitFit` using Coupled Fitting of the LDCs

Filter	Midwavelength (μm)	Bandwidth (μm)	R_p/R_*		u_0	u_1
			Fitted LDC	Fixed LDC		
g' band	0.467	0.139	0.0724 ± 0.0003	0.0724 ± 0.0003	0.857 ± 0.013	-0.063 ± 0.012
r' band	0.621	0.124	0.0700 ± 0.0002	0.0700 ± 0.0002	0.751 ± 0.012	-0.014 ± 0.012
i' band	0.754	0.130	0.0716 ± 0.0001	0.0717 ± 0.0001	0.669 ± 0.012	0.033 ± 0.011
z' band	0.940	0.256	0.0712 ± 0.0002	0.0713 ± 0.0003	0.655 ± 0.013	0.004 ± 0.012
R band	0.672	0.107	0.0698 ± 0.0002	0.0699 ± 0.0002	0.736 ± 0.013	0.002 ± 0.012
I band	0.805	0.289	0.0713 ± 0.0007	0.0717 ± 0.0008	0.679 ± 0.013	0.012 ± 0.012
TESS	0.745	0.400	0.0711 ± 0.0007	0.0716 ± 0.0008	0.587 ± 0.014	0.109 ± 0.013
HST/WFC3 G102	0.813	0.025	0.0713 ± 0.0004	0.0716 ± 0.0004	0.543 ± 0.007	0.073 ± 0.007
HST/WFC3 G102	0.838	0.025	0.0709 ± 0.0003	0.0710 ± 0.0003	0.534 ± 0.007	0.075 ± 0.007
HST/WFC3 G102	0.863	0.025	0.0706 ± 0.0004	0.0710 ± 0.0004	0.438 ± 0.009	0.120 ± 0.009
HST/WFC3 G102	0.888	0.025	0.0708 ± 0.0003	0.0709 ± 0.0003	0.428 ± 0.008	0.120 ± 0.008
HST/WFC3 G102	0.913	0.025	0.0709 ± 0.0003	0.0711 ± 0.0004	0.429 ± 0.009	0.115 ± 0.008
HST/WFC3 G102	0.938	0.025	0.0716 ± 0.0003	0.0716 ± 0.0004	0.414 ± 0.008	0.124 ± 0.008
HST/WFC3 G102	0.963	0.025	0.0717 ± 0.0002	0.0718 ± 0.0002	0.403 ± 0.005	0.117 ± 0.005
HST/WFC3 G102	0.988	0.025	0.0707 ± 0.0002	0.0709 ± 0.0002	0.379 ± 0.005	0.124 ± 0.006
HST/WFC3 G102	1.013	0.025	0.0704 ± 0.0003	0.0705 ± 0.0003	0.377 ± 0.007	0.126 ± 0.007
HST/WFC3 G102	1.038	0.025	0.0705 ± 0.0003	0.0707 ± 0.0003	0.364 ± 0.007	0.136 ± 0.008
HST/WFC3 G102	1.063	0.025	0.0704 ± 0.0003	0.0707 ± 0.0003	0.355 ± 0.007	0.132 ± 0.007
HST/WFC3 G102	1.088	0.025	0.0708 ± 0.0003	0.0711 ± 0.0003	0.365 ± 0.007	0.130 ± 0.007
HST/WFC3 G102	1.113	0.025	0.0712 ± 0.0002	0.0713 ± 0.0002	0.351 ± 0.005	0.131 ± 0.005
HST/WFC3 G102	1.138	0.025	0.0712 ± 0.0002	0.0713 ± 0.0003	0.343 ± 0.005	0.140 ± 0.005
HST/WFC3 G141	1.126	0.031	0.0711 ± 0.0002	0.0713 ± 0.0003	0.343 ± 0.006	0.138 ± 0.007
HST/WFC3 G141	1.156	0.029	0.0715 ± 0.0002	0.0717 ± 0.0002	0.337 ± 0.006	0.141 ± 0.007
HST/WFC3 G141	1.185	0.028	0.0712 ± 0.0002	0.0712 ± 0.0003	0.349 ± 0.006	0.128 ± 0.007
HST/WFC3 G141	1.212	0.027	0.0706 ± 0.0002	0.0708 ± 0.0003	0.338 ± 0.006	0.139 ± 0.007
HST/WFC3 G141	1.239	0.027	0.0703 ± 0.0002	0.0705 ± 0.0002	0.321 ± 0.005	0.153 ± 0.005
HST/WFC3 G141	1.266	0.027	0.0703 ± 0.0002	0.0704 ± 0.0002	0.320 ± 0.005	0.153 ± 0.005
HST/WFC3 G141	1.292	0.027	0.0705 ± 0.0002	0.0706 ± 0.0003	0.307 ± 0.007	0.169 ± 0.008
HST/WFC3 G141	1.319	0.026	0.0711 ± 0.0002	0.0712 ± 0.0003	0.299 ± 0.007	0.173 ± 0.008
HST/WFC3 G141	1.345	0.027	0.0718 ± 0.0002	0.0720 ± 0.0002	0.293 ± 0.007	0.174 ± 0.008
HST/WFC3 G141	1.372	0.027	0.0723 ± 0.0002	0.0723 ± 0.0002	0.285 ± 0.007	0.185 ± 0.008
HST/WFC3 G141	1.400	0.028	0.0726 ± 0.0002	0.0726 ± 0.0002	0.270 ± 0.005	0.199 ± 0.007
HST/WFC3 G141	1.428	0.029	0.0728 ± 0.0002	0.0729 ± 0.0002	0.259 ± 0.005	0.201 ± 0.007
HST/WFC3 G141	1.457	0.029	0.0726 ± 0.0002	0.0726 ± 0.0002	0.237 ± 0.007	0.229 ± 0.010
HST/WFC3 G141	1.487	0.031	0.0721 ± 0.0002	0.0721 ± 0.0002	0.224 ± 0.008	0.212 ± 0.010
HST/WFC3 G141	1.519	0.032	0.0715 ± 0.0002	0.0716 ± 0.0002	0.218 ± 0.008	0.223 ± 0.011
HST/WFC3 G141	1.551	0.034	0.0708 ± 0.0002	0.0708 ± 0.0003	0.214 ± 0.007	0.223 ± 0.010
HST/WFC3 G141	1.586	0.036	0.0702 ± 0.0002	0.0704 ± 0.0003	0.211 ± 0.008	0.222 ± 0.011
HST/WFC3 G141	1.624	0.039	0.0699 ± 0.0002	0.0700 ± 0.0003	0.211 ± 0.008	0.217 ± 0.010

publicly available for refitting, so only their published transit times can be used (as listed in Table 7). When added to the 33 transit times fitted with `TransitFit`, the combined 39 midtransit times were linearly fitted using the same MCMC procedure, resulting in the following revised linear ephemeris

$$T_m^c(E) = 2455304.65209_{-0.00030}^{+0.00030} + 4.234503_{-0.000001}^{+0.000001}E. \quad (4)$$

The MCMC posterior probability distribution for these 39 epochs is shown in Figure (B2). The best-fitting model shows $\chi_{\text{red}}^2 = 46$ with 37 degrees of freedom and $\text{BIC} = 1713$. Using the ephemeris from this linear fitting, another $O - C$ diagram was constructed, shown in Figure 10.

4.2. The Frequency Analysis of TTVs

The previous TTV analysis of HAT-P-26 b by von Essen et al. (2019) found cyclic variation with a period of

~ 270 epochs. In this work, we reinvestigate the TTVs using the timing from our refitting result in Table 7. The generalized Lomb–Scargle (GLS) periodogram (Zechmeister & Kürster 2009) from the `PyAstronomy`²³ routines (Czesla et al. 2019) was used to search for periodicity in the timing residual data.

First, we performed a GLS analysis on our 33 refitted timing residuals based on Equation (3). The result is shown as a periodogram in Figure 9(a). In this periodogram, the highest-power peak has a strength of 0.7882 at a frequency of 0.0045 ± 0.0001 cycles period⁻¹ ($\simeq 222$ epochs) with a false alarm probability (FAP) of $1 \times 10^{-7}\%$.

The frequency of the highest-power peak is assumed to be the frequency of the cyclic TTV of the system. In order to find the amplitude of the cyclic variation, the same procedure as described in von Essen et al. (2019) is used. The timing

²³ `PyAstronomy`: <https://github.com/sczesla/PyAstronomy>.

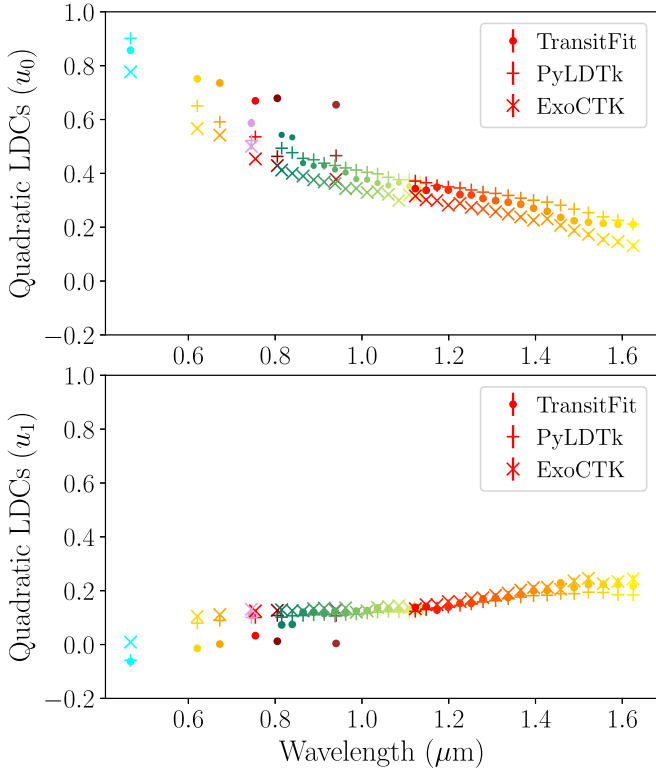


Figure 7. The LDCs were calculated from TransitFit, PyLDTk, and ExoCTK. The colors of the bandpass filters are the same as those in Figures 5 and 6.

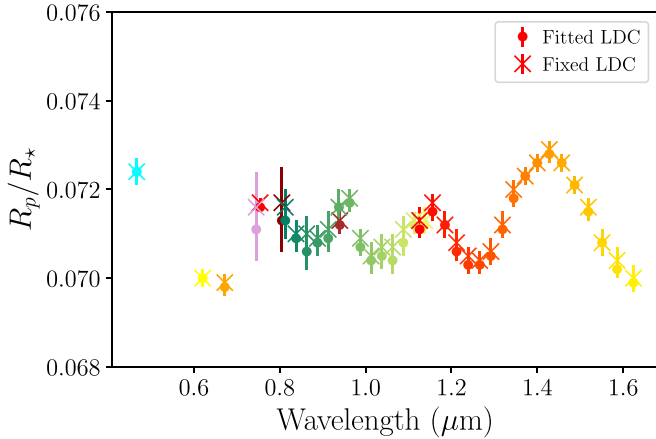


Figure 8. The planetary radii calculated from both models with fitted LDCs and fixed LDCs. The colors of the bandpass filters are the same as those in Figures 5 and 6.

residuals were fitted through the function

$$\text{TTV}(E) = A_{\text{TTV}} \sin(2\pi fE - \phi), \quad (5)$$

where A_{TTV} is the amplitude (in minutes) of the timing perturbation, f is the frequency on the highest peak of the power periodogram, and ϕ is the orbital phase at $E = 0$. From the fitting, an amplitude of $A_{\text{TTV}} = 1.98 \pm 0.05$ minutes and an initial orbital phase of $\phi = -0.22 \pm 0.04$ is obtained. The best-fitting model provides $\chi_{\text{red}}^2 = 4.2$ and $\text{BIC} = 136.2$. The timing residuals with the best fit of sinusoidal variability are plotted in Figure 9(b). This period is much shorter than the period obtained by von Essen et al. (2019).

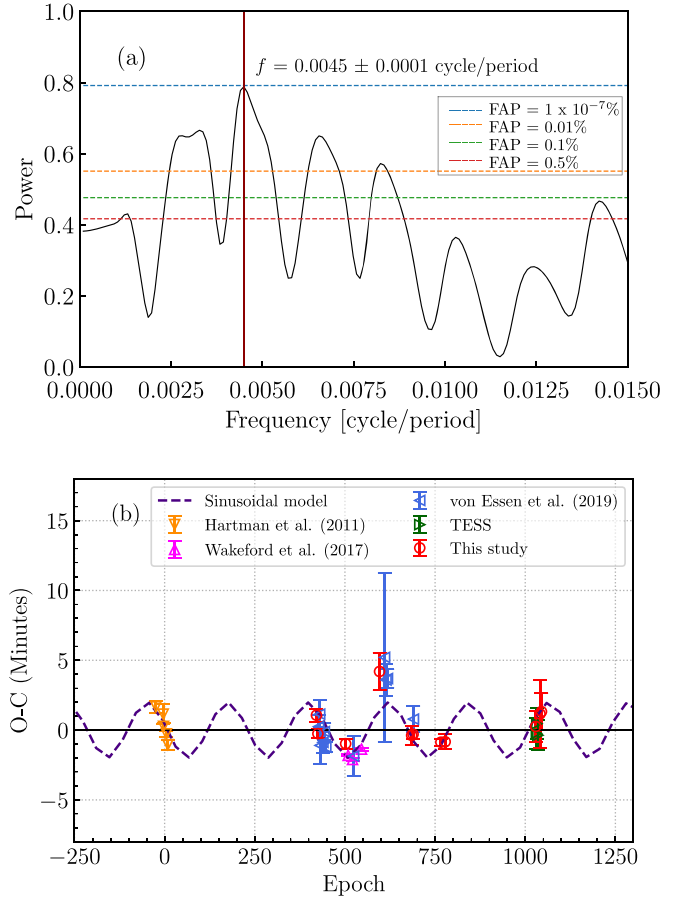


Figure 9. (a) GLS periodogram for the timing residuals of the 33 midtransit times obtained from TransitFit. The dashed lines indicate the FAP levels. (b) $O - C$ diagram and the best fit of the sinusoidal variability from the frequency of the highest-power peak, where $\text{FAP} = 1 \times 10^{-7}\%$ (purple dashed line).

The difference in the TTV periods might be caused by differences in our data sets. There are six transit times in von Essen et al. (2019)'s analysis (one transit time from Hartman et al. 2011; four transit times from Stevenson et al. 2016; and one transit time from Wakeford et al. 2017), which have not been used in this work, as their raw light curves have yet to be published. In order to answer whether these six transit times affect the TTV periodicity, we also perform the GLS analysis on the combined set of 39 epochs, using the ephemeris of Equation (4).

The GLS analysis for these 39 epochs detects three periodicity peaks with $\text{FAP} 3 \times 10^{-13}\%$, shown in Figure 10(a). The three corresponding best-fit sinusoidal functions are shown in Table 9. The timing residuals with the best-fit sinusoidal variability for each power peak detection are plotted in Figure 10(b). From these three power peaks, there is a peak with a frequency of 0.0045 ± 0.0001 cycles period $^{-1}$, which has a frequency similar to the frequency of the power peak of the 33 TransitFit refitted timing. The other two peak frequencies, f_1 and f_3 , could be harmonics of this frequency (f_2). Therefore, the HAT-P-26 b timing is consistent with a sinusoidal variation with a frequency of 0.0045 ± 0.0001 cycles period $^{-1}$.

There are many possible causes of the TTV signal. For example, stellar activity (Rabus et al. 2009; Barros et al. 2013) or gravitational interactions with an additional planet in the system. The variations due to stellar activity are likely to be

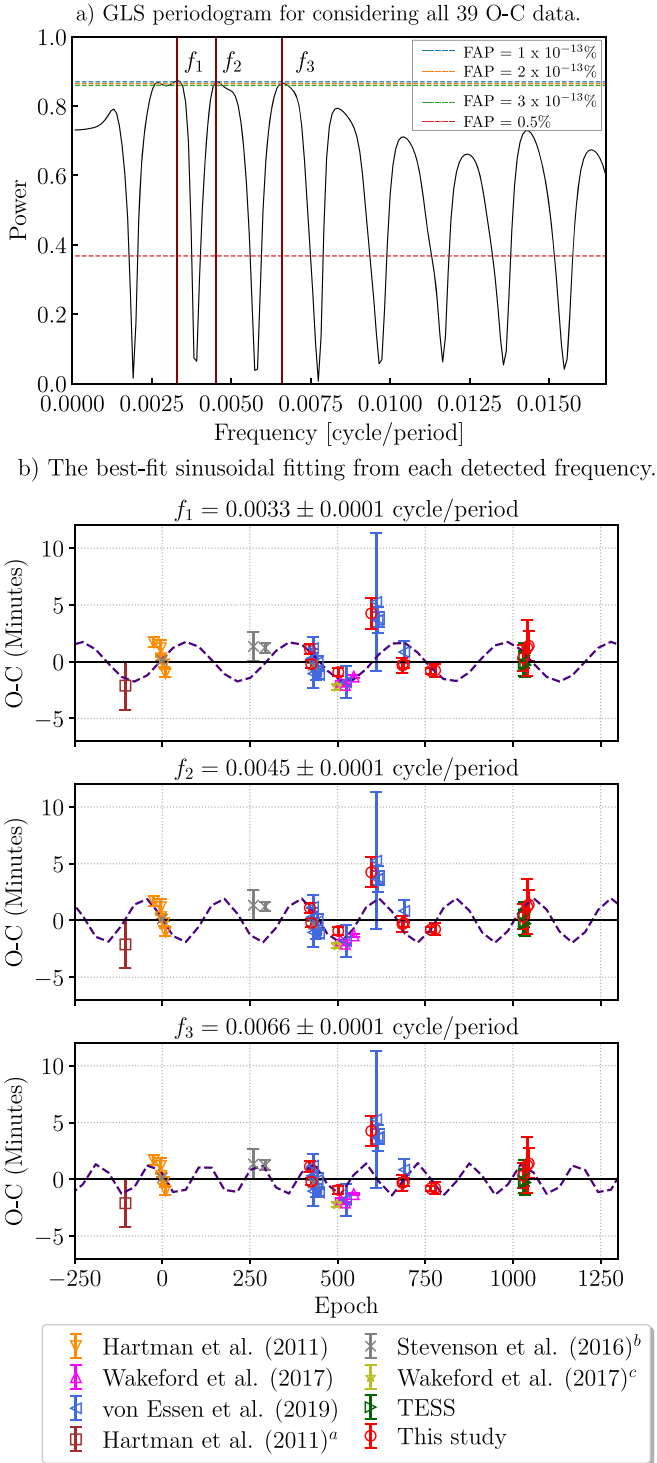


Figure 10. (a) GLS periodogram of timing residuals of all 39 midtransit times, showing three peaks with $\text{FAP} < 3 \times 10^{-13}\%$. The dashed lines indicate the FAP levels. (b) $O - C$ diagram and the best-fit sinusoid for the detected frequencies f_1 (top), f_2 (middle), and f_3 (bottom; purple dashed line). **Notes:** *a*: the midtransit times (T_m) are adopted from the transit light curve observed by HATNet field 376 (Hartman et al. 2011); *b*: T_m adopted from Stevenson et al. (2016); and *c*: T_m adopted from the transit light curves observed by HST/STIS (Wakeford et al. 2017).

ruled out as von Essen et al. (2019) show that there is no spot modulation within the precision limit of the data within three years. We therefore instead consider the possibility of the presence of an additional planet.

Given the frequency of 0.0045 ± 0.0001 cycles period⁻¹, and the assumption of a coplanar orbit, we model an additional exoplanet with an orbital period near the first-order resonance of HAT-P-26 b. In the case of a first-order mean-motion resonance, $j:j - 1$, Lithwick et al. (2012) allows us to calculate the additional planet mass as

$$V = P \frac{\mu'}{\pi j^{2/3} (j-1)^{1/3} \Delta} \left(-f - \frac{3 Z_{\text{free}}^*}{2 \Delta} \right), \quad (6)$$

where V is the amplitude of TTV (from our analysis, $V = 1.98$ minutes), P is the orbital period of HAT-P-26 b, μ' is the outer-planet mass, Δ is the normalized distance to the resonance, f is the sum of the Laplace coefficients with order-unity values, and Z_{free}^* is a dynamical quantity that controls the TTV signal. From the analysis, if an additional planet has 2:1 orbital resonance with HAT-P-26 b (i.e. $P \sim 8.47$ days), we find that the mass of the additional planet could be around $0.02 M_{\text{Jup}}$ ($6.36 M_{\oplus}$).

5. Atmospheric Modeling

Previous studies of HAT-P-26 b via near-infrared transmission spectroscopy found a significant detection of H_2O in the atmosphere (Stevenson et al. 2016; Wakeford et al. 2017; MacDonald & Madhusudhan 2019). The optical analysis by MacDonald & Madhusudhan (2019) found evidence of metal hydrides, with three potential candidates identified as TiH, CrH, and ScH. The derived temperature from their study was 563_{-55}^{+59} K, with a temperature gradient of ~ 80 K. To confirm the presence of metal hydrides in the optical and the H_2O at near-infrared wavelengths, we reinvestigated the chemical composition of HAT-P-26 b's atmosphere using the combined spectrophotometry from the optical ground-based observations and the optical/near-infrared observations by HST. Our fitted R_p/R_* values using TransitFit are consistent with the values provided by Wakeford et al. (2017) in both the optical and near-infrared wave bands as shown in Figure 13.

Retrieval of the transmission spectrum was performed using the open-source atmospheric retrieval framework TauREx 3²⁴ (Al-Refaie et al. 2021) using the nested-sampling routines from MultiNest (Feroz et al. 2009) with 1000 live points. The 38 transit depths from Table 8 are used to retrieve planetary atmospheric compositions. The stellar parameters and the planet mass were adopted from Hartman et al. (2011). The stellar emission spectrum was simulated using a PHOENIX model (Husser et al. 2013) for a star of $T_* = 4700$ K. We adopted an isothermal temperature profile and a parallel plane atmosphere of 100 layers, with pressure ranging from 10^{-1} to 10^6 Pa with logarithmic spacing.

In keeping with MacDonald & Madhusudhan (2019), we modeled the molecular opacities of metal hydrides, including TiH (Burrows et al. 2005), CrH (Burrows et al. 2002), and ScH (Lodi et al. 2015). We also added the presence of the following active trace gases: TiO (McKemmish et al. 2019), VO (McKemmish et al. 2016), K and Na (Allard et al. 2019), MgH (Owens et al. 2022), SiH (Yurchenko et al. 2018), N_2 (Western et al. 2018), O_2 (Somogyi et al. 2021), and H_2O (Polyansky et al. 2018), and the inactive gases He/ H_2 (Abel et al. 2012). The molecular line lists are taken from the ExoMol (Tennyson et al. 2016), HITRAN (Gordon et al. 2016), and HITEMP (Rothman & Gordon 2014) databases. We also

²⁴ TauREx 3: https://github.com/ucl-exoplanets/TauREx3_public/.

Table 9
The Detected Frequencies with the Best-fit Parameters of the Sinusoidal Functions, Considering all 39 Midtransit times

Frequencies (cycles period ⁻¹)	Power	FAP	A_{TTV} (minutes)	ϕ	χ_{red}^2	BIC
$f_1 = 0.0033 \pm 0.0001$	0.873	$1 \times 10^{-13}\%$	1.75 ± 0.05	-0.13 ± 0.02	6.69	254.72
$f_2 = 0.0045 \pm 0.0001$	0.871	$2 \times 10^{-13}\%$	1.95 ± 0.05	3.23 ± 0.02	6.13	233.95
$f_3 = 0.0066 \pm 0.0001$	0.867	$3 \times 10^{-13}\%$	1.42 ± 0.06	-0.36 ± 0.03	22.65	845.39

Table 10
The Parameters and Priors Used for TauREx 3 Retrieval, and the Best-fit Retrieved Parameters, Based on Fitting Only the HST/WFC3 Data from Both MacDonald & Madhusudhan (2019) and TransitFit, and Based on Fitting All Available Data Sets

Parameter	Priors	Scale	Published Value HST/WFC3 MacDonald et al. (2019)	Retrieved Value		
				HST/WFC3 MacDonald et al. (2019)	HST/WFC3 TransitFit	All TransitFit
R_p (R_{Jup})	(0.5, 0.6)	linear	...	$0.570^{+0.005}_{-0.009}$	$0.561^{+0.007}_{-0.008}$	$0.564^{+0.005}_{-0.006}$
T (K)	(400, 1200)	linear	563^{+59}_{-55}	560^{+90}_{-60}	590^{+50}_{-50}	590^{+60}_{-50}
H ₂ O	(-4, -0.2)	log	$-1.83^{+0.39}_{-0.43}$	$-1.5^{+0.4}_{-0.5}$	$-2.0^{+0.6}_{-0.5}$	$-1.6^{+0.3}_{-0.3}$
TiO	(-12, -1)	log	...	-11^{+1}_{-1}	$-9.0^{+0.6}_{-0.7}$	-10^{+1}_{-1}
VO	(-12, -1)	log	...	-9^{+1}_{-2}	$-8.7^{+0.6}_{-0.6}$	$-8.9^{+0.6}_{-0.7}$
Na	(-12, -1)	log	...	-7^{+3}_{-3}	-7^{+4}_{-4}	-6^{+3}_{-4}
K	(-12, -1)	log	...	-7^{+3}_{-3}	-7^{+4}_{-4}	-7^{+4}_{-4}
ScH	(-12, -1)	log	$-4.76^{+0.91}_{-4.09}$	-7^{+3}_{-3}	-7^{+4}_{-4}	-7^{+4}_{-3}
TiH	(-12, -1)	log	$-6.24^{+0.71}_{-0.65}$	-7^{+3}_{-3}	-7^{+4}_{-4}	-7^{+3}_{-4}
CrH	(-12, -1)	log	$-5.72^{+0.89}_{-1.37}$	-7^{+3}_{-3}	-7^{+4}_{-4}	-7^{+3}_{-3}
MgH	(-12, -1)	log	...	-8^{+3}_{-3}	-8^{+3}_{-3}	-6^{+3}_{-3}
SiH	(-12, -1)	log	...	-7^{+3}_{-3}	-7^{+3}_{-3}	-6^{+3}_{-4}
N ₂	(-12, -1)	log	...	-7^{+3}_{-3}	-7^{+4}_{-4}	-6^{+3}_{-4}
O ₂	(-12, -1)	log	...	-7^{+3}_{-3}	-7^{+4}_{-4}	-7^{+3}_{-3}
He/H ₂	(-3, -0.04)	log	-0.77	$-1.6^{+0.9}_{-0.9}$	$-1.2^{+0.5}_{-0.5}$	$-1.0^{+0.3}_{-0.4}$
P_{clouds} (Pa)	(1, 5)	log	>0.72	$3.9^{+0.6}_{-0.8}$	$3.9^{+0.6}_{-0.7}$	$4.2^{+0.5}_{-0.6}$

include collision-induced absorption between H₂ molecules (Abel et al. 2011; Fletcher et al. 2018) and between H₂ and He (Abel et al. 2012) in the transmission spectrum model. A list of the parameters used in the TauREx 3 retrieval is shown in Table 10.

The modeling results are shown in Table 10, and Figures 11 and 13. HAT-P-26 b's atmosphere is modeled to have a 100 Pa temperature of 590^{+60}_{-50} K, which is cooler than the estimated equilibrium temperature (≈ 1000 K; Hartman et al. 2011). This temperature is compatible with the calculated 100 Pa temperature of MacDonald & Madhusudhan (2019; 563^{+59}_{-55} K). Combining the result with our cloud-top pressure at $P_{\text{cloud}} > 10^3$ Pa, HAT-P-26 b can be assumed to have a cloud- and haze-free atmosphere with an He/H₂ ratio of 0.1. The ratio indicates that H₂ dominates the atmosphere. The transmission analysis suggests a water abundance of $2.4^{+3.0}_{-1.6}\%$ of the volume mixing ratio. While, the other modeled chemical compositions should represent less than 0.01% of the volume mixing ratio of the atmosphere.

To compare our result to MacDonald & Madhusudhan (2019), which uses the same HST/WFC3 data, we employed TauREx 3 to model the transmission spectra exclusively from the HST/WFC3 observations. Figures 12 and 14 show that this model retrieves an H₂O abundance of $1.0^{+2.9}_{-0.6}\%$, which is similar to the abundance obtained by MacDonald & Madhusudhan (2019; $1.5^{+2.1}_{-0.9}\%$ H₂O). Furthermore, both models also provide the same atmospheric temperature at 100 Pa (590 K). However, our analysis does not provide any

evidence for the presence of metal hydrides, as reported by MacDonald & Madhusudhan (2019).

The discrepancy observed may be attributed to the absence of HST/Space Telescope Imaging Spectrograph (STIS) transits and Spitzer transits in our atmospheric modeling, which were used in MacDonald & Madhusudhan (2019). We have not include them as we were unable to obtain the raw light curves. Simply adding the published HST/STIS and Spitzer transit depths to our atmospheric analysis would not be a suitable solution, since those depths result from different physical parameters (orbital period, semimajor axis, and inclination). However, when we modeled the transmission spectra of MacDonald & Madhusudhan (2019) using TauREx 3, we also obtained the same chemical abundance as reported by MacDonald & Madhusudhan (2019), who used the POSEIDON code (MacDonald & Madhusudhan 2017) as the retrieval model (Table 10). Therefore, the nondetection of metal hydrides in this work is not led by the difference atmospheric retrieval models.

Nevertheless, the reported detections of metal hydrides by MacDonald & Madhusudhan (2019) still exhibit low abundance levels (less than 0.01% abundance), making it challenging to confirm their presence definitively. However, the retrieved abundance in our analysis remains within the 1σ error bars of the results obtained by MacDonald & Madhusudhan (2019). Furthermore, it should be noted that we have not included the optical spectra data from the Magellan Low Dispersion Survey Spectrograph 3 and HST/STIS G750L observations, which were used in the analysis conducted by MacDonald & Madhusudhan (2019).

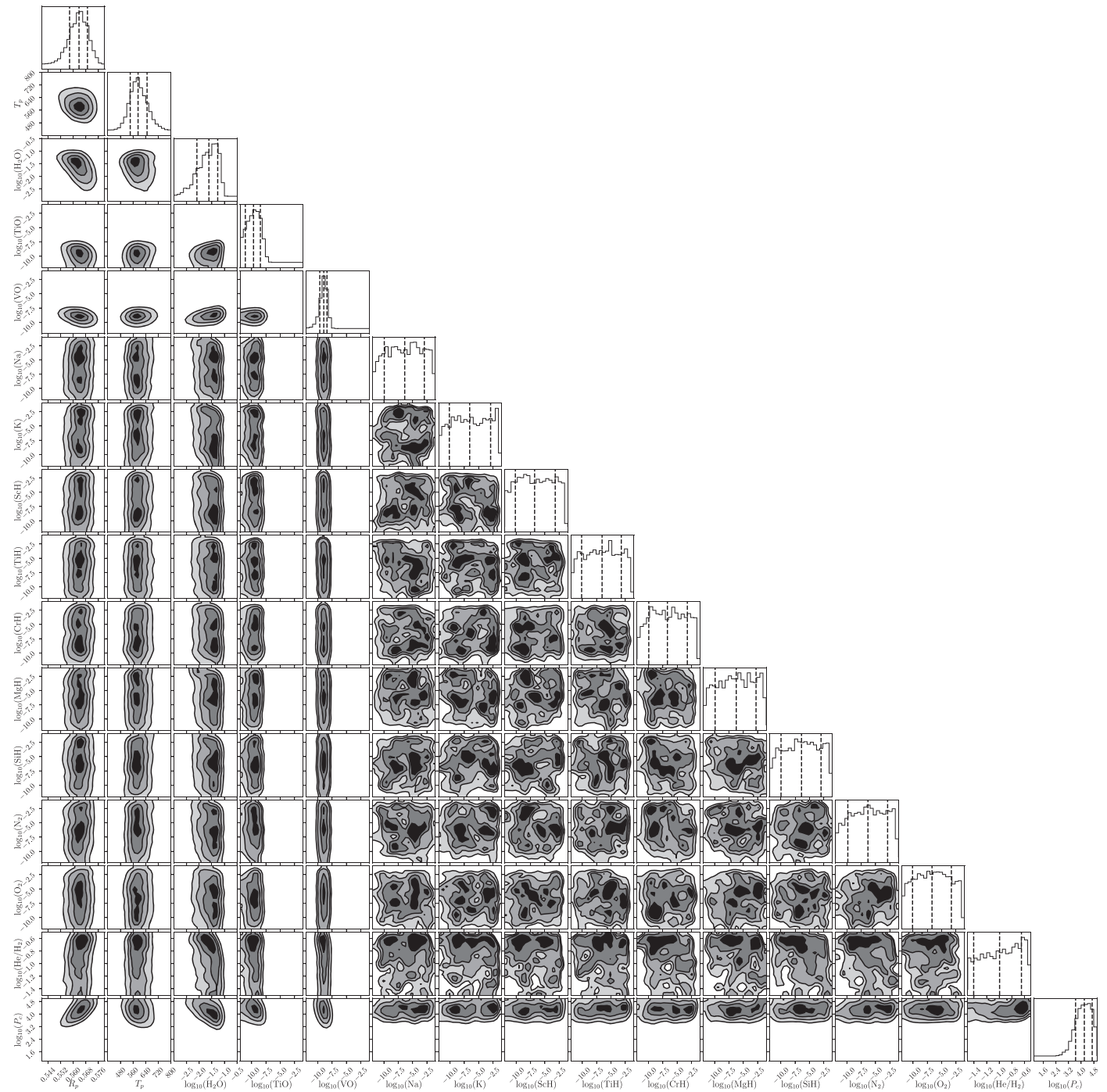


Figure 11. Posterior probability distribution for our HAT-P-26 b atmospheric model, using nested sampling and the TauREx 3 package.

Since the strongest metal hydride features identified by MacDonald & Madhusudhan (2019) occur within the Magellan and HST bandpasses, our exclusion of these data may explain why we obtain nondetections.

6. Discussion and Conclusions

This work performs multiband photometric follow-up observations of the Neptune-mass planet HAT-P-26 b, using a range of space- and ground-based data, including new data gathered from the SPEARNET telescope network. A total of 13 new transit light curves were combined with published light

curves from HST, TESS, and ground-based telescopes, to model the physical parameters of HAT-P-26 b using the TransitFit light-curve analysis package.

By fitting these observations, we derived the following parameters of HAT-P-26 b: an inclination of $i = 87.83^\circ \pm 0.05^\circ$, a star–planet separation of $12.49 \pm 0.07 R_*$, plus the midtransit times for each transit event and the planet-to-star radius ratio (R_p/R_*) for each filter. Limb-darkening parameters for the HST/WFC3 G102 and G104 grism data are compatible with the computed values from ExoCTK. However, the fitted optical LDCs from TransitFit show inconsistency with the ExoCTK calculated values.

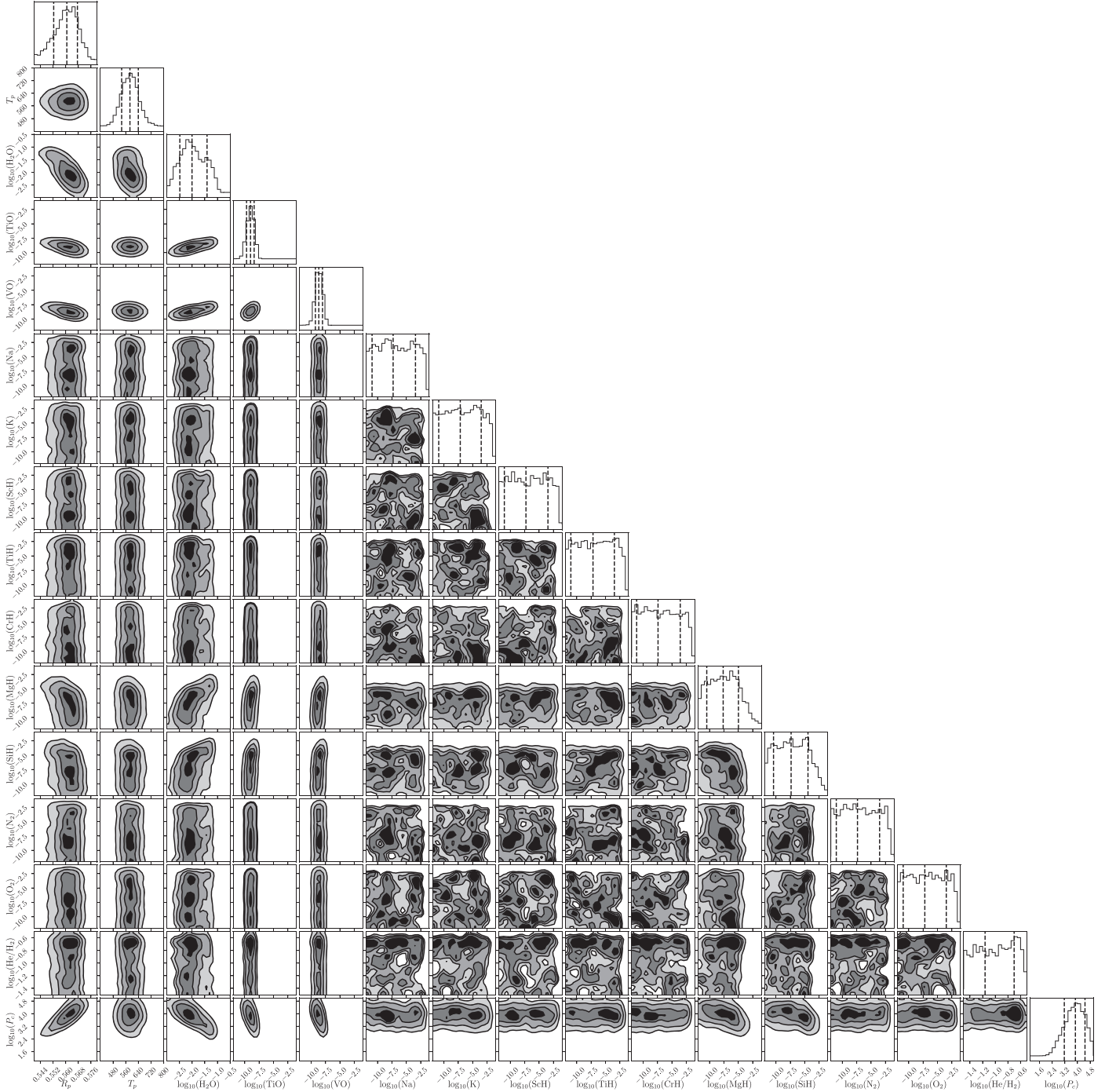


Figure 12. Posterior probability distribution for our HAT-P-26 b atmospheric model, calculated using only the HST/WFC3 data, via nested sampling with TauREx 3.

Based on the midtransit times from the 33 epochs obtained from *TransitFit*, we refined the linear ephemeris, finding $T_m^c(E) = 2455304.65211^{+0.00036}_{-0.00035} + E 4.234503^{+0.000001}_{-0.000001}$. We performed a periodogram analysis to search for TTV signals that might be caused by an additional planet in the HAT-P-26 system. A TTV amplitude of 1.98 ± 0.05 minutes was detected with a frequency of 0.0045 ± 0.0001 cycles period⁻¹, equivalent to a sinusoidal period of $\simeq 222$ epochs. This is shorter than the period presented by von Essen et al. (2019; $\simeq 270$ epochs). If the TTV amplitude is due to the presence of a third-body orbit that is near the first-order resonance of HAT-P-26 b (~ 8.47 days), its mass could be around $0.02 M_{\text{Jup}}$ ($6.36 M_{\oplus}$).

The atmospheric composition of HAT-P-26 b is modeled using the transit depths obtained from the *TransitFit* package and analyzed with *TauREx 3*. At a pressure of 100 Pa, HAT-P-26 b exhibits an atmospheric temperature of 590^{+60}_{-50} K, with a cloud-top pressure estimated to be $P_c > 10^4$ Pa. The abundance of H₂O in HAT-P-26 b's atmosphere is determined to be $2.4^{+3.0}_{-0.6}\%$ of the volume mixing ratio, which aligns with the abundance reported by MacDonald & Madhusudhan (2019). Although other modeled chemical components are expected to contribute less than 0.01% to the volume mixing ratio in the overall atmosphere and they do not indicate clear evidence in support of the presence of metal hydrides as

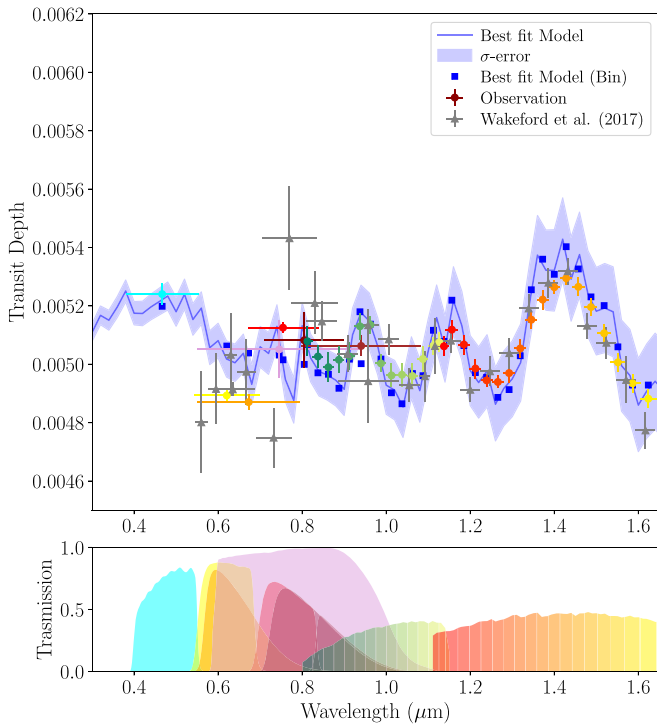


Figure 13. Top panel: the best-fit transmission spectrum of HAT-P-26 b, calculated using ground-based, TESS, and the HST/WFC3 data from *TransitFit*, with synthetic models generated by *TauREx 3* (blue solid line), with their 1σ errors (blue bands). The blue squares are the binned best-fit transmission spectra. The gray stars are the transmission spectra obtained by Wakeford et al. (2017). The observed data are binned using the bandpass in the bottom panel.

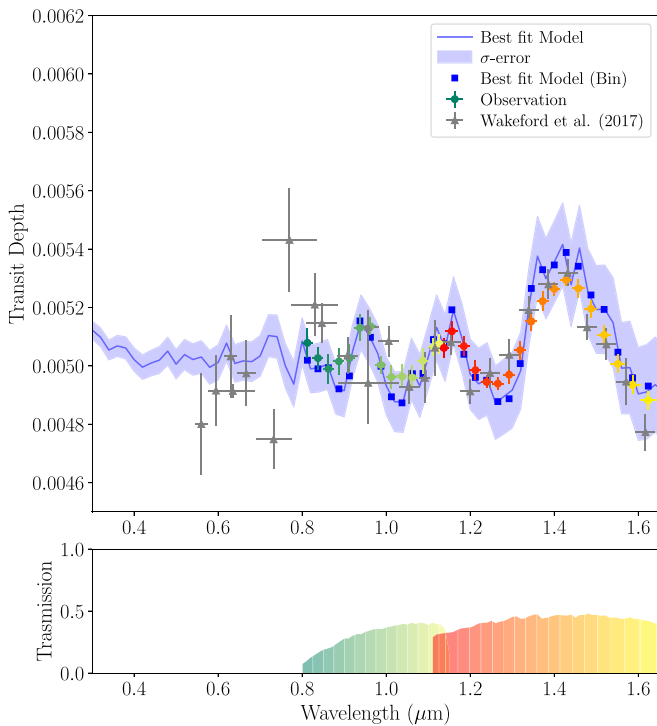


Figure 14. Top panel: the best-fit transmission spectrum of HAT-P-26 b, based on fitting only the HST/WFC3 data from *TransitFit* with synthetic models generated by *TauREx 3* (blue solid line), with their 1σ errors (blue bands). The blue squares are the binned best-fit transmission spectra. The data are binned using the bandpass in the bottom panel.

reported by MacDonald & Madhusudhan (2019), our analysis yields an abundance within the 1σ error range of MacDonald & Madhusudhan (2019). This discrepancy in the detection/nondetection is not attributed to differences in the atmospheric retrieval models used. Nevertheless, the absence of detected metal hydrides in our study could still be attributed to differences in the optical spectra used for the analysis in our work and in the study by MacDonald & Madhusudhan (2019).

Acknowledgments

We are grateful to the anonymous referee for their useful suggestions, which help to improve this paper significantly. This work is based on observations made with ULTRASPEC at the Thai National Observatory and the Thai Robotic Telescopes operated by the National Astronomical Research Institute of Thailand (Public Organization). The data used in this work also included the available data based on observations with the NASA/ESA Hubble Space Telescope (HST), obtained at the Space Telescope Science Institute (STScI) operated by AURA, Inc. The publicly available HST observations presented here were taken as part of proposal 14260, led by PI: Drake Deming and proposal 14110, led by PI: David Sing. These were obtained from the Hubble archive. Additionally, this work included data collected by the TESS mission, whose funding was provided by the NASA Explorer Program. HST and TESS data presented in this paper were obtained from the Mikulski Archive for Space Telescopes (MAST) at STScI. The specific observations analyzed can be accessed via [10.17909/pmhe-db52](https://archive.stsci.edu/missions/tess/10.17909/pmhe-db52) and [10.17909/t9-nmc8-f686](https://archive.stsci.edu/missions/tess/10.17909/t9-nmc8-f686). This research made use of the open-source Python package *ExoCTK*, the Exoplanet Characterization Toolkit (Bourque et al. 2021).

This work presents results from the European Space Agency (ESA) space mission Gaia. Gaia data are being processed by the Gaia Data Processing and Analysis Consortium (DPAC). Funding for the DPAC is provided by national institutions, in particular the institutions participating in the Gaia MultiLateral Agreement (MLA). The Gaia mission website is <https://www.cosmos.esa.int/gaia>. The Gaia archive website is <https://archives.esac.esa.int/gaia>. We thank Angelos Tsiaras and Quentin Chaignat for the suggestion on *Iraclis* and the instruction of *TauREx*.

This work is supported by the grant from the National Science and Technology Council, Taiwan. The grant numbers are MOST 109-2112-M-007-007, MOST 110-2112-M-007-035, and MOST 111-2112-M-007-035. This work is also partially supported by National Astronomical Research Institute of Thailand (Public Organization) research grant.

Facilities: HST/WFC3 (G141 and G102), TESS, 2.4 m (TNT), 0.5 m (TRT-TNO), 0.7 m (TRT-GAO), and 0.7 m (TRT-SRO)

Software: *SExtractor* (Bertin & Arnouts 1996), *Astrometry.net* (Lang et al. 2010), *TransitFit* (Hayes et al. 2021), *Iraclis* (Tsiaras et al. 2016a), and *TauREx* (Al-Refaie et al. 2021).

Appendix A

Individual SPEARNET Transit Light Curves

Individual SPEARNET transit light curves of HAT-P-26 b from the observations in 2015–2018 are presented here as Figures A1 and A2.

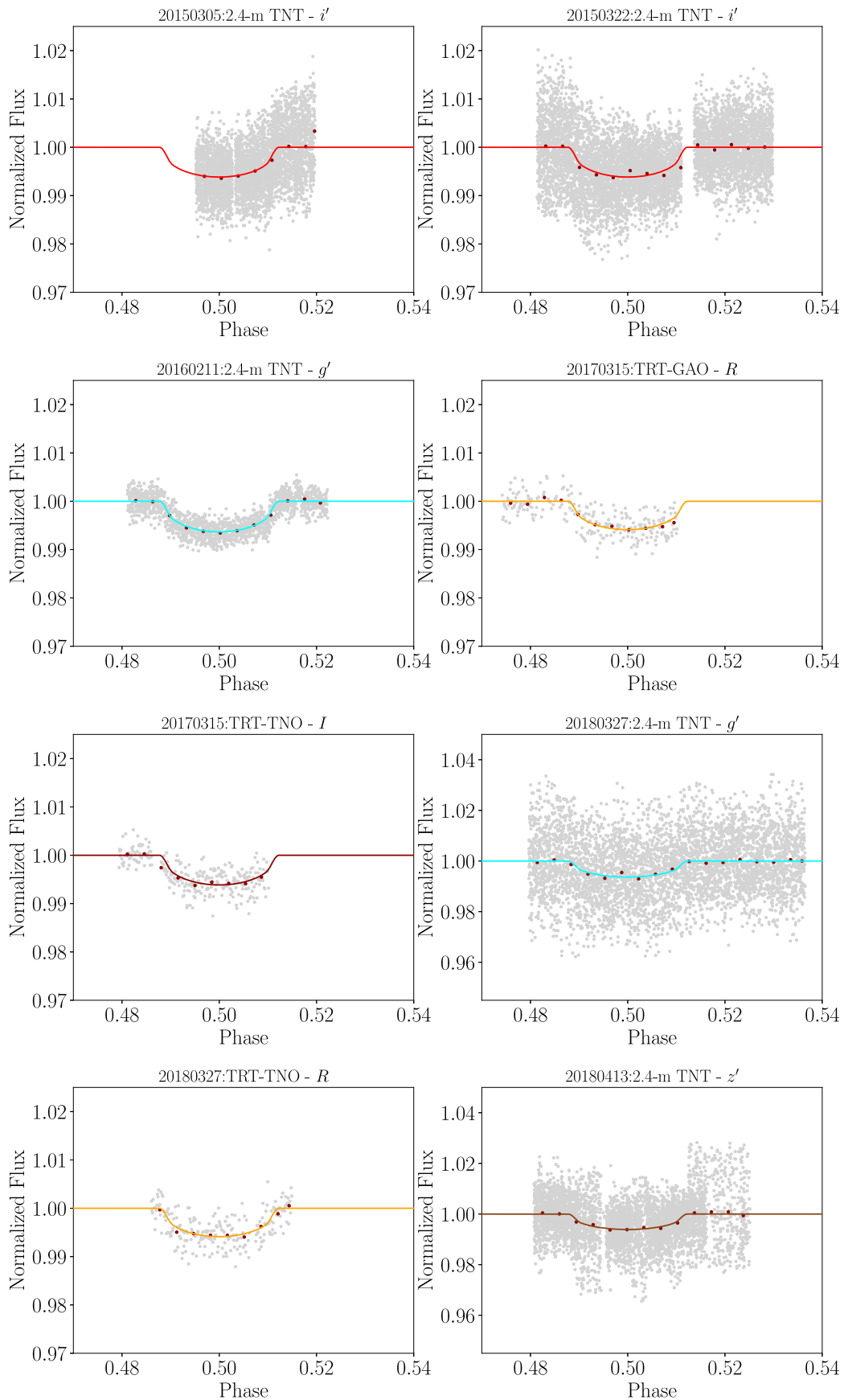


Figure A1. Individual SPEARNET transit light curves of HAT-P-26 b from observations in 2015–2018. The light curves are normalized (gray dots) and modeled by `TransitFit` (solid lines). The light curves are observed in the g' (blue), r' (yellow), R (orange), i' (red), I (dark red), and z' (brown) filters. 5 minute binned light curves are shown by the red dots.

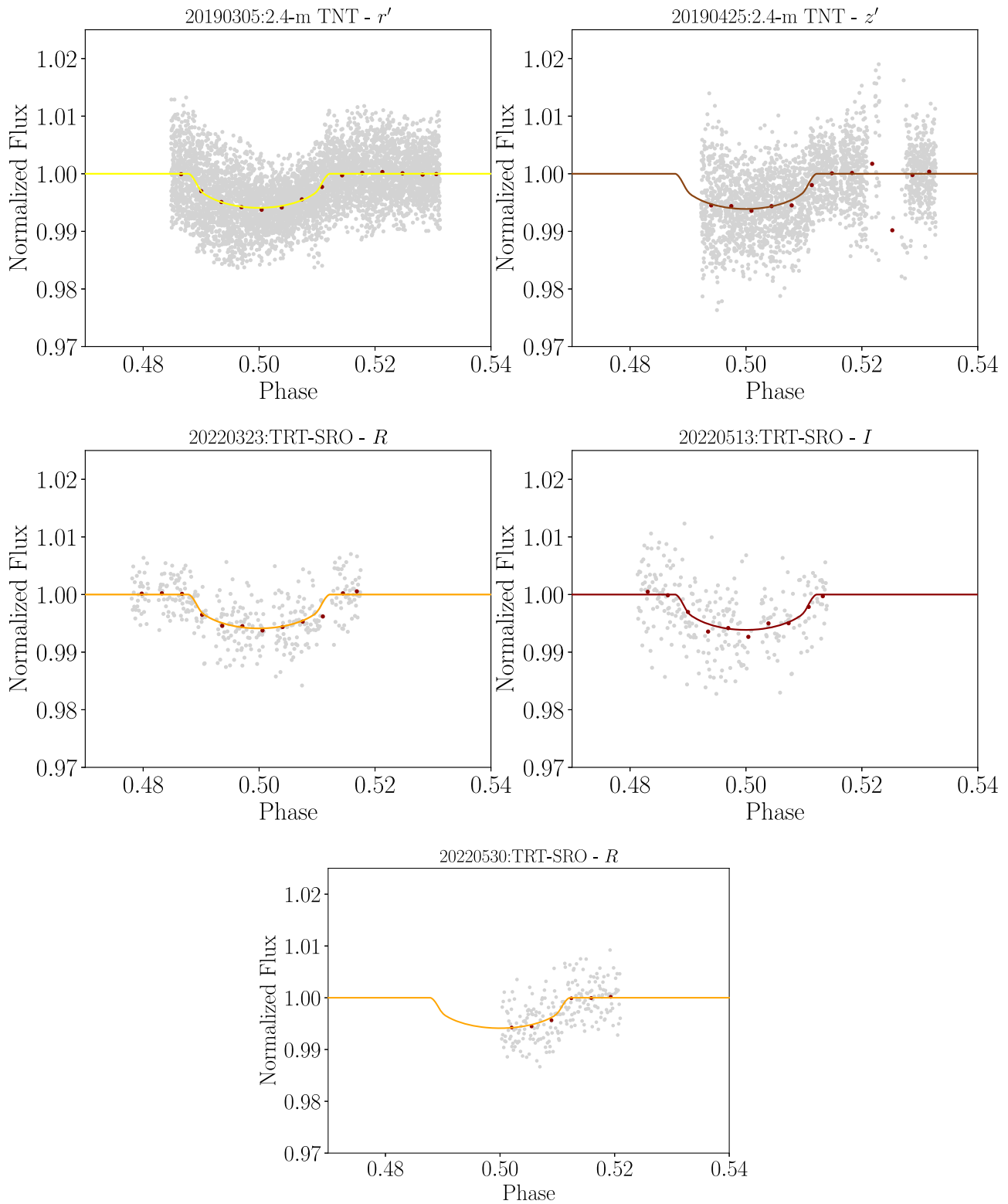


Figure A2. Individual SPEARNET transit light curves of HAT-P-26 b from observations in 2015–2018. The light curves are normalized (gray dots) and modeled by `TransitFit` (solid lines). The light curves are observed in the g' (blue), r' (yellow), R (orange), i' (red), I (dark red), and z' (brown) filters. 5 minute binned light curves are shown by the red dots.

Appendix B

Posterior Probability Distribution for the Linear Ephemeris Model MCMC Fitting Parameters

Here we present posterior probability distributions of the linear ephemeris MCMC fitting parameters as Figures B1 and B2.

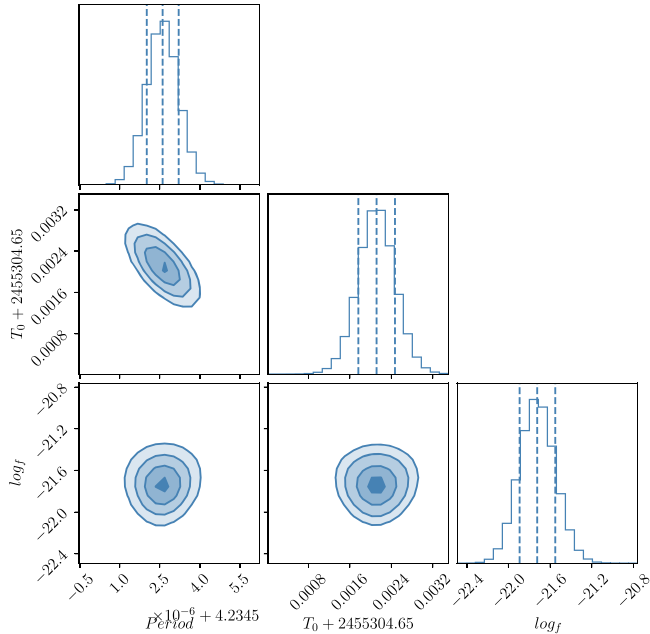


Figure B1. Posterior probability distribution of the linear ephemeris MCMC fitting parameters for the 33 midtransit times obtained from *TransitFit*.

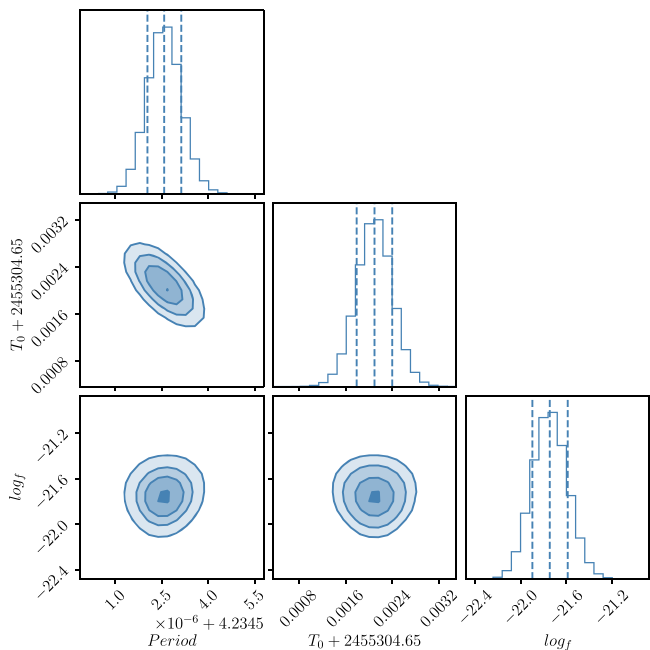


Figure B2. Posterior probability distribution of the linear ephemeris MCMC fitting parameters for considering all 39 midtransit times.

ORCID iDs

Napaporn A-thano <https://orcid.org/0000-0001-7234-7167>
Supachai Awiphan <https://orcid.org/0000-0003-3251-3583>

Ing-Guey Jiang <https://orcid.org/0000-0001-7359-3300>
Eamonn Kerins <https://orcid.org/0000-0002-1743-4468>
Akshay Priyadarshi <https://orcid.org/0000-0003-1143-0877>
Iain McDonald <https://orcid.org/0000-0003-0356-0655>
Yogesh C. Joshi <https://orcid.org/0000-0001-8657-1573>
Chung-Kai Huang <https://orcid.org/0000-0003-0728-1493>
Li-Chin Yeh <https://orcid.org/0000-0001-8677-0521>

References

- Abel, M., Frommhold, L., Li, X., & Hunt, K. L. C. 2011, *JPCA*, **115**, 6805
Abel, M., Frommhold, L., Li, X., & Hunt, K. L. C. 2012, *JChPh*, **136**, 044319
Agol, E., & Fabrycky, D. C. 2018, in *Handbook of Exoplanets*, ed. H. J. Deeg & J. A. Belmonte (New York: Springer), 7
Agol, E., Steffen, J., Sari, R., & Clarkson, W. 2005, *MNRAS*, **359**, 567
Allard, F. 2014, in *IAU Symp. 299, Exploring the Formation and Evolution of Planetary Systems*, ed. M. Booth, B. C. Matthews, & J. R. Graham (Cambridge: Cambridge Univ. Press), 271
Allard, F., Homeier, D., & Freytag, B. 2011, in *ASP Conf. Ser. 448, 16th Cambridge Workshop on Cool Stars, Stellar Systems, and the Sun*, ed. C. Johns-Krull, M. K. Browning, & A. A. West (San Francisco, CA: ASP), 91
Allard, N. F., Spiegelman, F., Leininger, T., & Molliere, P. 2019, *A&A*, **628**, A120
Al-Refaie, A. F., Changeat, Q., Waldmann, I. P., & Tinetti, G. 2021, *ApJ*, **917**, 37
Bakos, G., Afonso, C., Henning, T., et al. 2009, in *IAU Symp. 253, Transiting Planets* (Cambridge: Cambridge Univ. Press), 354
Bakos, G., Noyes, R. W., Kovács, G., et al. 2004, *PASP*, **116**, 266
Barros, S. C. C., Boué, G., Gibson, N. P., et al. 2013, *MNRAS*, **430**, 3032
Bertin, E., & Arnouts, S. 1996, *A&AS*, **117**, 393
Borucki, W. J., Koch, D., Basri, G., et al. 2005, *A Decade of Extrasolar Planets Around Normal Stars* (Cambridge: Cambridge Univ. Press), 36
Bourque, M., Espinoza, N., Filippazzo, J., et al. 2021, *The Exoplanet Characterization Toolkit (ExoCTK), 1.0.0*, Zenodo, doi:10.5281/zenodo.4556063
Brande, J., Crossfield, I. J. M., Kreidberg, L., et al. 2022, *AJ*, **164**, 197
Burrows, A., Dulick, M., & Bauschlicher, C. W. 2005, *ApJ*, **624**, 988
Burrows, A., Ram, R. S., Bernath, P., Sharp, C. M., & Milsom, J. A. 2002, *ApJ*, **577**, 986
Burt, J. A., Dragomir, D., Mollière, P., et al. 2021, *AJ*, **162**, 87
Claret, A. 2000, *A&A*, **363**, 1081
Claret, A. 2004, *A&A*, **428**, 1001
Czesla, S., Schröter, S., Schneider, C. P., et al. 2019, *PyA: Python Astronomy-related Packages*, Astrophysics Source Code Library, ascl:1906.010
Dhillon, V. S., Marsh, T. R., Atkinson, D. C., et al. 2014, *MNRAS*, **444**, 4009
Edwards, B., Changeat, Q., Mori, M., et al. 2021, *AJ*, **161**, 44
Feroz, F., Hobson, M. P., & Bridges, M. 2009, *MNRAS*, **398**, 1601
Fletcher, L. N., Gustafsson, M., & Orton, G. S. 2018, *ApJS*, **235**, 24
Foreman-Mackey, D., Hogg, D. W., Lang, D., & Goodman, J. 2013, *PASP*, **125**, 306
Fulton, B. J., Shporer, A., Winn, J. N., et al. 2011, *AJ*, **142**, 84
Glidic, K., Schlawin, E., Wisner, L., et al. 2022, *AJ*, **164**, 19
Gordon, I., Rothman, L. S., Wilzewski, J. S., et al. 2016, *DPS*, **48**, 421.13
Hartman, J. D., Bakos, G. Á., Kipping, D. M., et al. 2011, *ApJ*, **728**, 138
Hayes, J. J. C., Kerins, E., Morgan, J. S., et al. 2021, arXiv:2103.12139
Husser, T. O., Wende-von Berg, S., Dreizler, S., et al. 2013, *A&A*, **553**, A6
Jenkins, J. M., Twicken, J. D., McCauliff, S., et al. 2016, *Proc. SPIE*, **9913**, 99133E
Kanodia, S., & Wright, J. 2018, *RNAAS*, **2**, 4
Kreidberg, L. 2015, *PASP*, **127**, 1161
Kreidberg, L., Bean, J. L., Désert, J.-M., et al. 2014, *ApJL*, **793**, L27
Kreidberg, L., Line, M. R., Parmentier, V., et al. 2018b, *AJ*, **156**, 17
Kreidberg, L., Line, M. R., Thorngren, D., Morley, C. V., & Stevenson, K. B. 2018a, *ApJL*, **858**, L6
Lang, D., Hogg, D. W., Mierle, K., Blanton, M., & Roweis, S. 2010, *AJ*, **139**, 1782
Lithwick, Y., Xie, J., & Wu, Y. 2012, *ApJ*, **761**, 122
Lodi, L., Yurchenko, S. N., & Tennyson, J. 2015, *MolPh*, **113**, 1998
MacDonald, R. J., & Madhusudhan, N. 2017, *MNRAS*, **469**, 1979
MacDonald, R. J., & Madhusudhan, N. 2019, *MNRAS*, **486**, 1292
McDonald, I., van Loon, J. T., Decin, L., et al. 2009, *MNRAS*, **394**, 831
McDonald, I., Zijlstra, A. A., & Boyer, M. L. 2012, *MNRAS*, **427**, 343
McDonald, I., Zijlstra, A. A., & Watson, R. A. 2017, *MNRAS*, **471**, 770

- McKemmish, L. K., Masseron, T., Hoeijmakers, H. J., et al. 2019, *MNRAS*, **488**, 2836
- McKemmish, L. K., Yurchenko, S. N., & Tennyson, J. 2016, *MNRAS*, **463**, 771
- Owens, A., Dooley, S., McLaughlin, L., et al. 2022, *MNRAS*, **511**, 5448
- Parviainen, H., & Aigrain, S. 2015, *MNRAS*, **453**, 3821
- Pepper, J., Pogge, R. W., DePoy, D. L., et al. 2007, *PASP*, **119**, 923
- Pollacco, D. L., Skillen, I., Collier Cameron, A., et al. 2006, *PASP*, **118**, 1407
- Polyansky, O. L., Kyuberis, A. A., Zobov, N. F., et al. 2018, *MNRAS*, **480**, 2597
- Pontoppidan, K. M., Barrientes, J., Blome, C., et al. 2022, *ApJL*, **936**, L14
- Rabus, M., Alonso, R., Belmonte, J. A., et al. 2009, *A&A*, **494**, 391
- Rauer, H., Catala, C., Aerts, C., et al. 2014, *ExA*, **38**, 249
- Ricker, G. R., Winn, J. N., Vanderspek, R., et al. 2014, *Proc. SPIE*, **9143**, 914320
- Rothman, L. S., & Gordon, I. E. 2014, in 13th Int. HITRAN Conf. (Cambridge, MA: Harvard Univ. Press), 49
- Rustamkulov, Z., Sing, D. K., Mukherjee, S., et al. 2023, *Natur*, **614**, 659
- Seager, S., & Deming, D. 2010, *ARA&A*, **48**, 631
- Seager, S., & Sasselov, D. D. 2000, *ApJ*, **537**, 916
- Smith, A. M. S. 2014, *CoSka*, **43**, 500
- Smith, J. C., Morris, R. L., Jenkins, J. M., et al. 2017a, Kepler Data Processing Handbook KSCI-19081-002, 7
- Smith, J. C., Stumpe, M. C., Jenkins, J. M., et al. 2017b, Kepler Data Processing Handbook KSCI-19081-002, 8
- Somogyi, W., Yurchenko, S. N., & Yachmenev, A. 2021, *JChPh*, **155**, 214303
- Speagle, J. S. 2020, *MNRAS*, **493**, 3132
- Stevenson, K. B., Bean, J. L., Seifahrt, A., et al. 2016, *ApJ*, **817**, 141
- Tennyson, J., Yurchenko, S. N., Al-Refaie, A. F., et al. 2016, *JMoSp*, **327**, 73
- Tinetti, G., Drossart, P., Eccleston, P., et al. 2018, *ExA*, **46**, 135
- Tody, D. 1986, *Proc. SPIE*, **627**, 733
- Tody, D. 1993, in ASP Conf. Ser. 52, Astronomical Data Analysis Software and Systems II, ed. R. J. Hanisch, R. J. V. Brissenden, & J. Barnes (San Francisco, CA: ASP)
- Trifonov, T., Brahm, R., Espinoza, N., et al. 2021, *AJ*, **162**, 283
- Tsiaras, A., Rocchetto, M., Waldmann, I. P., et al. 2016a, *ApJ*, **820**, 99
- Tsiaras, A., Waldmann, I. P., Rocchetto, M., et al. 2016b, *ApJ*, **832**, 202
- von Essen, C., Wedemeyer, S., Sosa, M. S., et al. 2019, *A&A*, **628**, A116
- Wakeford, H. R., Sing, D. K., Kataria, T., et al. 2017, *Sci*, **356**, 628
- Western, C. M., Carter-Blatchford, L., Crozet, P., et al. 2018, *JQSRT*, **219**, 127
- Wheatley, P. J., West, R. G., Goad, M. R., et al. 2018, *MNRAS*, **475**, 4476
- Wittrock, J. M., Dreizler, S., Reefe, M. A., et al. 2022, *AJ*, **164**, 27
- Yurchenko, S. N., Szabó, I., Pyatenko, E., & Tennyson, J. 2018, *MNRAS*, **480**, 3397
- Zechmeister, M., & Kürster, M. 2009, *A&A*, **496**, 577